Modeling multicomponent ionic transport in groundwater with IPhreeqc coupling: Electrostatic interactions and geochemical reactions in homogeneous and heterogeneous domains

Muniruzzaman, Muhammad; Rolle, Massimo

Published in:
Advances in Water Resources

Link to article, DOI:
10.1016/j.advwatres.2016.10.013

Publication date:
2016

Document Version
Peer reviewed version

This is a Post Print of the article published on line 13th October 2016 in Advances in Water Resources and printed December 2016, 98, 1-15. The publishers' version is available at the permanent link: http://dx.doi.org/10.1016/j.advwatres.2016.10.013

Modeling multicomponent ionic transport in groundwater with IPhreeqc coupling: electrostatic interactions and geochemical reactions in homogeneous and heterogeneous domains

Muhammad Muniruzzaman[1] and Massimo Rolle[1,2*]

[1]Center for Applied Geosciences, University of Tübingen, Hölderlinstr. 12, D-72074 Tübingen, Germany

[2]Department of Environmental Engineering, Technical University of Denmark, Miljøvej, Building 115, 2800 Kgs. Lyngby, Denmark

[*]Corresponding author phone: +45 45251566; email: masro@env.dtu.dk

Highlights

- 2-D code for multicomponent ionic transport including Coulombic interactions.
- Geochemical reactions implemented with IPhreeqc coupling.
- Applications in physically and chemically heterogeneous domains.

ABSTRACT

The key role of small-scale processes like molecular diffusion and electrochemical migration has been increasingly recognized in multicomponent reactive transport in saturated porous media. In this study, we propose a two-dimensional multicomponent reactive transport model taking into account the electrostatic interactions during transport of charged ions in physically and chemically heterogeneous porous media. The modeling approach is based on the local charge balance and on the description of compound-specific and spatially variable diffusive/dispersive fluxes. The multicomponent ionic transport code is coupled with the geochemical code PHREEQC-3 by utilizing the IPhreeqc module, thus enabling to perform the geochemical calculations included in the PHREEQC's reaction package. The multicomponent reactive transport code is benchmarked with different 1-D and 2-D transport problems. Successively, conservative and reactive transport examples are presented to demonstrate the capability of the proposed model to simulate transport of charged species in heterogeneous porous media with spatially variable physical and chemical properties. The results reveal that the Coulombic cross-coupling between dispersive fluxes can significantly influence conservative as well as reactive transport of charged species both at the laboratory and at the field scale.

Keywords: *multicomponent diffusion, electrochemical migration, IPhreeqc coupling, Coulombic interactions, reactive transport modeling*

1. INTRODUCTION

The importance of coupling subsurface solute transport models with geochemical codes, capable of simulating a wide variety of equilibrium and kinetic reactions, has been increasingly recognized and has led to major developments of reactive transport codes for subsurface environmental simulation (e.g., [1,2]). The coupling of fluid flow, mass transport and geochemical reactions is instrumental for understanding and predicting the complex interplay between physical and bio-geochemical processes in sediments and groundwater systems, as well as for the quantitative interpretation of experimental observations both at the laboratory and field scales. Combining flow and transport codes with geochemical reaction packages has led to a first generation of now well-established reactive transport simulators for both groundwater (e.g., CrunchFlow [3]; Geochemist's Workbench [4]; PHT3D [5]; PHAST [6]) and unsaturated/multiphase flow (e.g., HYDROGEOCHEM [7]; TOUGHREACT [8-10]; MIN3P [11]). Developments have continued over the last decade with increasing capabilities added to existing simulators as well as new couplings between different transport and geochemical codes (e.g. HP1/HPx [12]; PHWAT [13]; RICH-PHREEQC [14]). Impetus to such advances was certainly provided by the release of modules such as IPhreeqc [15] and PhreeqcRM [16] devised to increase the flexibility in interfacing the widely used USGS's geochemical reaction package PHREEQC [17,18] with other codes. In particular, IPhreeqc is a C++ PHREEQC module designed for coupling PHREEQC's reaction capabilities (e.g., equilibrium reactions, ion exchange, surface complexation, solid solutions, mineral dissolution and precipitation, as well as kinetic reactions both abiotic and microbially mediated) to other software programs (for example, MATLAB®, Excel®, Visual Basic®)

and/or programming and scripting languages (for instance, C, C++, FORTRAN, Python, R). IPhreeqc offers a wide range of extensive features to combine multidimensional transport simulators with comprehensive geochemistry packages including thermodynamic databases [19,20]. Recent reactive transport simulators that benefited from the IPhreeqc capabilities include the couplings with COMSOL Multiphysics® (e.g., [19]; [21,22]), OpenGeoSys [23,24] and UTCHEM [25].

In this study we also take advantage of the IPhreeqc capabilities to explore the coupling between a two-dimensional multicomponent ionic formulation of charged species advective-dispersive transport and reactive processes. Many studies have demonstrated the importance of electrostatic effects due to charge interactions and leading to multicomponent diffusion of ions in aqueous solutions. Experimental observations have shown the effects of Coulombic interactions on the diffusive mobility of major ions, heavy metals and radioactive tracers both at the laboratory [26,27] and at the field scale [28-31]. The description of such interactions in multicomponent diffusion models is usually treated by including an electromigration term in addition to the classical Fickian diffusion term (e.g., [32-36]). In a series of recent laboratory flow-through experiments we have shown that the role of Coulombic effects is critical not only in diffusion-dominated systems but also in advection-dominated flow regimes [37-39]. In fact, the results of such experiments demonstrated that the displacement of ions in porous media is coupled and the electromigration effects do not vanish at high flow velocities. These experimental findings represent a challenge as well as an opportunity for further development of reactive transport codes. Only recently a dataset of multicomponent conservative ionic transport obtained under flow-through conditions in a homogeneous

porous medium has been used to benchmark the multicomponent transport capabilities of the CrunchFlow and MIN3P codes [40]. However, to the best of our knowledge, the behavior and effects of Coulombic interactions for multidimensional conservative and reactive transport in physically and chemically heterogeneous porous media have not been investigated, yet. The purpose of this contribution is to present a reactive transport tool helping to address these issues in particular on the light of the increased recognition of the key role of molecular diffusion for solute transport from the pore to the field scale. Small scale diffusive processes have been shown to impact solute transport in flow-through systems not only at the laboratory (e.g., [41-45]) but also at the larger field scale (e.g., [46-54]). The impact of diffusion, which is the only true mixing process in groundwater [55], on solute transport indeed does not vanish at larger scales but propagates through scales also under flow-through conditions [53]. Models aiming at capturing these effects in heterogeneous flow fields need to implement improved and more realistic descriptions of local dispersion, linking the mechanical dispersion term to spatially-variable hydraulic conductivity values and avoiding using constant dispersivities that inevitably mask (or underestimate) the role of aqueous diffusion in porous media.

This work presents a two-dimensional reactive transport model that explicitly accounts for the Coulombic interactions coupled with geochemical reactions during multicomponent ionic transport in both homogeneous and heterogeneous flow-fields under transient transport conditions. The modeling approach is based on a charge-balanced multicomponent formulation and on the spatially variable description of local hydrodynamic dispersion that is of key importance for the coupling of the fluxes of the different ionic species in solution. Additionally, we couple the two-dimensional

multicomponent ionic transport model with the widely used geochemical code PHREEQC (version 3, [18]) by using the reaction module IPhreeqc [15]. Thus, the proposed numerical reactive-transport model provides a comprehensive framework that is based on the novel combination of three specific features: (i) detailed description of spatially variable local hydrodynamic dispersion, (ii) multicomponent ionic formulation; and (iii) extensive reaction capabilities through the coupling with PHREEQC. These features represent distinctive and unique characteristics for a reactive transport simulator and are particularly advantageous for performing transport simulations in physically and chemically heterogeneous domains. The 2-D multicomponent model is systematically benchmarked with the analytical solution of a 2-D transport problem, with experimental data, and with 1-D reactive transport scenarios solved in PHREEQC. Successively, application examples, with different levels of complexity, are presented to illustrate transient multicomponent ionic transport and the influence of charge interactions in both conservative and reactive systems in homogeneous and heterogeneous porous media.

2. MULTICOMPONENT IONIC TRANSPORT

The most distinguishing feature of aqueous diffusion of charged species compared to non-charged solutes is the electrostatic interactions between the dissolved charged species and/or with charged interfaces. Multicomponent ionic diffusion models are generally used to account for these inter-species interactions during diffusive movement of charged species at different scales (e.g., [27-29]; [32,33]; [35]; [56-59]). These models, based on Nernst-Planck formulations, are typically derived from the chemical potential

expressions by following a pragmatic extension of Fick's law (e.g., [35,36,60]). Therefore, the multicomponent diffusive movement of a charged species in electrolyte systems can be expressed as [29,36]:

$$J_i = -D_i \nabla C_i - D_i C_i \nabla \ln \gamma_i - D_i \frac{z_i F}{RT} C_i \nabla \Phi \quad i = 1, 2, 3, ..., N \tag{1}$$

where D_i is the self-diffusion coefficient, C_i is the concentration of charged species i, γ_i is the activity coefficient, z_i is the charge number, F is the Faraday's constant, R is the ideal gas constant, T is the temperature, Φ is the electrostatic potential, and N is the number of species.

In dilute solutions and in the absence of strong ionic strength gradients, the gradient of the activity coefficients (second term of Eq. 1) can be neglected [33]. Thus, the above expression describing the multicomponent ionic diffusive fluxes reduces to:

$$J_i = -D_i \nabla C_i - D_i \frac{z_i F}{RT} C_i \nabla \Phi \tag{2}$$

This equation includes fluxes due to self-diffusion as well as electromigration, which is basically induced from the electrostatic interactions, for a particular mobile species. Following two physical constraints based on electroneutrality (i.e., (i) conservation of local charge balance, $\sum_{i=1}^{N} z_i C_i = 0$ and/or (ii) zero influx of electrical current, $\sum_{i=1}^{N} z_i J_i = 0$), the gradient of Φ can be expressed as:

$$\nabla\Phi = \frac{\sum_{i=1}^{N}\left(z_i D_i \nabla C_i\right)}{\sum_{i=1}^{N}\left(z_i^2 F D_i C_i\right)\Big/ RT} \tag{3}$$

128 Therefore, the flux expression of Eq. (2) readily reduces to:

$$J_i = -D_i \nabla C_i + \frac{z_i D_i C_i}{\sum_{j=1}^{N}\left(z_j^2 D_j C_j\right)} \sum_{k=1}^{N}\left(z_k D_k \nabla C_k\right) \tag{4}$$

129 This formulation directly describes the movement of a particular charged species as a
130 function of concentration gradients, self-diffusion coefficients, and charge numbers not
131 only of that ion but also of all ionic species in the electrolyte system. Eq. (4) can also be
132 further rearranged in a more compact notation that takes the form:

$$J_i = -\sum_{j=1}^{N}\left(D_{ij} \nabla C_j\right) \tag{5}$$

133 where D_{ij} are the inter-diffusion coefficients that include both the pure diffusive (first
134 term, Eq. 4) and the electromigration (second term, Eq. 4) fluxes. The cross-coupled
135 inter-diffusion coefficients are defined as:

$$D_{ij} = \delta_{ij} D_i - \frac{z_i z_j D_i D_j C_i}{\sum_{k=1}^{n}(z_k^2 D_k C_k)} \tag{6}$$

136 where δ_{ij} is the Kronecker delta that is equal to 1 when $i=j$ and equal to 0 if $i \neq j$.

137 In flow-through systems an analogous set of equations (Eqs. 1-6) can be derived by
138 following the above steps and replacing the pure self-diffusion coefficients by the
139 hydrodynamic dispersion coefficients [37,38].

3. MODELING APPROACH

The proposed model is implemented in MATLAB® and allows for steady-state flow, transient multicomponent advective-dispersive transport and geochemical reactions, the latter performed with the IPhreeqc coupling. Fig. 1 schematically illustrates the structure of the multicomponent reactive transport code. Details on the model capabilities, in particular the multicomponent ionic transport features and the coupling with the geochemical reaction package, are discussed in the sections below.

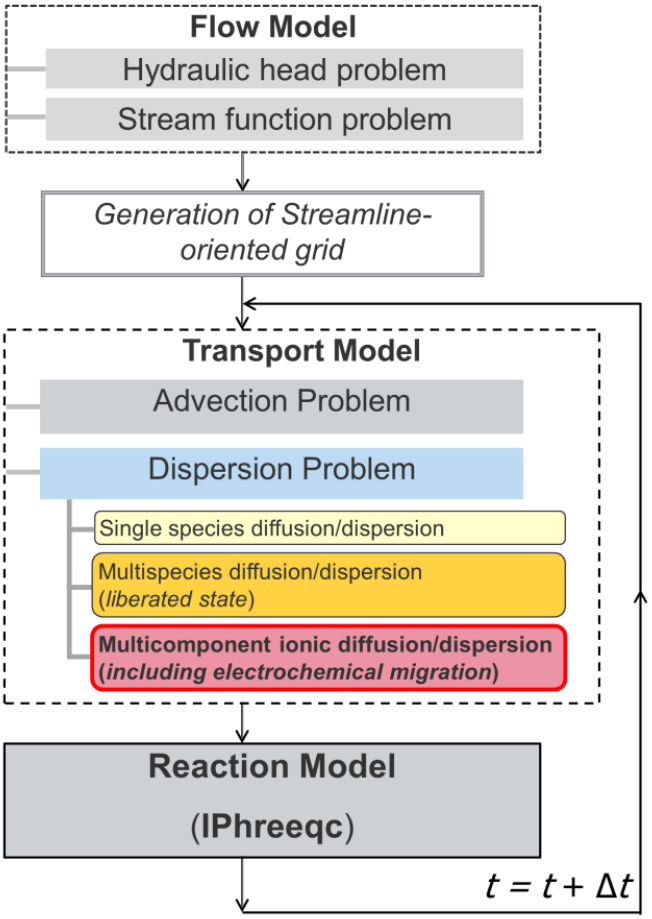

Figure 1: Schematic diagram of the structure of the multicomponent reactive transport model.

3.1 Solution of Flow and Transport Equations

The governing equation for steady-state groundwater flow in a two-dimensional domain is expressed as [61]:

$$\nabla \cdot \left(\mathbf{K} \nabla h \right) = 0$$
$$\nabla \cdot \left(\mathbf{K}^{-1} \nabla \psi \right) = 0 \tag{7}$$

where h, ψ and $\mathbf{K}$ are hydraulic head, stream function and hydraulic conductivity tensor, respectively. The groundwater flow problem (Eq. 7) is solved numerically by bilinear finite elements on rectangular grid.

The governing equation for multicomponent ionic transport problem coupled with reactive processes in two-dimensional saturated porous media reads as:

$$\frac{\partial C_i}{\partial t} = -\boldsymbol{v} \cdot \nabla C_i + \nabla \cdot \left(\sum_{j=1}^{N} \mathbf{D}_{ij} \nabla C_j \right) - R_i \tag{8}$$

where t is time, $\boldsymbol{v}$ is the seepage velocity vector, $\mathbf{D}_{ij}$ is the tensor for cross-coupled dispersion coefficients, R_i is the reactive source/sink term. For charged compounds the entries of $\mathbf{D}_{ij}$ in a two-dimensional local coordinate system, referencing along the directions parallel and orthogonal to flow, are described as:

$$\mathbf{D}_{ij} = \begin{bmatrix} \mathbf{D}_{ij}^{L} & 0 \\ 0 & \mathbf{D}_{ij}^{T} \end{bmatrix} \tag{9}$$

in which $\mathbf{D}_{ij}^{L}$ and $\mathbf{D}_{ij}^{T}$ are the matrices of longitudinal and transverse cross-coupled dispersion coefficients [38], respectively. These cross-coupled terms, which allow accounting for the flux of a charged species driven by both its own concentration gradient

and the electrical field created by the movement of other ions present in solution, are in fact analogous to inter-diffusion coefficients in Eq. (6) and can be expressed as:

$$\mathbf{D}_{ij}^{L} = \delta_{ij} D_i^{L} - \frac{z_i z_j D_i^{L} D_j^{L} C_i}{\sum_{k=1}^{N} \left(z_k^2 D_k^{L} C_k \right)}$$
$$\mathbf{D}_{ij}^{T} = \delta_{ij} D_i^{T} - \frac{z_i z_j D_i^{T} D_j^{T} C_i}{\sum_{k=1}^{N} \left(z_k^2 D_k^{T} C_k \right)} \quad (10)$$

where D_i^L and D_i^T are the longitudinal and transverse hydrodynamic self-dispersion coefficient of species *i* (i.e., when a particular ion is "liberated" from the other charged species in solution). The hydrodynamic dispersion coefficients, which are important parameters for the realistic description of dispersive transport, are parameterized by using the linear relationship proposed by Guedes de Carvalho and Delgado [62] for longitudinal dispersion and a non-linear compound-specific relationship [50,63] for the transverse component:

$$D_i^{L} = D_i^{P} + \frac{1}{2} v d$$
$$D_i^{T} = D_i^{P} + D_i^{aq} \left(\frac{Pe_i^2}{Pe_i + 2 + 4\delta^2} \right)^{\beta} \quad (11)$$

where D_i^{aq} is the aqueous diffusion coefficient, $D_i^P = D_i^{aq} / \tau$ is the pore diffusion coefficient and τ the tortuosity of the porous medium. Since the latter is difficult to determine, the pore diffusion coefficient is typically described as a function of the porosity (θ) and a common approximation for unconsolidated material is $D_i^P \approx \theta D_i^{aq}$ (e.g., Archie [64]; Boving and Grathwohl[65]). *d* is the average grain size diameter and

Pe_i ($= vd / D_i^{aq}$; with v being the flow velocity) is the grain Péclet number of species i. δ denotes the ratio between the length of a pore channel to its hydraulic radius. β is an empirical exponent that accounts for the effects of incomplete mixing in the pore channels. The parameterizations of D_i^L and D_i^T in Eq. 11 were selected because they have been validated and extensively supported by experimental data from controlled flow-through experiments. Other parameterizations such as the classic model of Scheidegger [66] as well as more complex models of local dispersion obtained for instance from pore-scale analysis and suggesting a weak non-linearity also of the longitudinal component [67] can be readily implemented. An important feature for high-resolution transport simulations in heterogeneous porous media is to take into account that the grain diameter (d) in Eq. (11) is spatially variable and should be linked to the local hydraulic conductivity value. We use the simple approximation of Hazen [68], which was adopted in previous studies (e.g., [51,69]), as a relationship between the grain diameter and hydraulic conductivity:

$$d \approx c\sqrt{K} \tag{12}$$

with the empirical proportionality constant c = 0.01 $m^{0.5}s^{0.5}$. This approach ensures a greatly improved representation of local dispersion compared to the common practice of considering constant dispersivities even in highly heterogeneous formations. The spatially variable hydrodynamic self-dispersion coefficients are of critical importance in the electrostatic cross-coupling between charged species and allow providing a detailed description of multicomponent ionic transport in heterogeneous formations.

The multicomponent transport problem (Eq. 8) is solved numerically on streamline-oriented grids following the method of Cirpka et al. [61]. The use of such grids, constructed based on the results of the flow simulation, reduces numerical errors by minimizing artificial dispersion. The advective-dispersive term is computed with the cell-centered finite volume method (FVM) [70]. We use a sequential non-iterative operator splitting approach to decouple the transport and reaction terms. For the advection problem, we use upwind differentiation for spatial discretization and the explicit Euler method for time integration. The dispersive fluxes are computed by the implicit Euler method for integration in time. The resulting system of equations for the dispersion problem is solved by using the direct matrix solver UMFPACK [71]). In multicomponent ionic transport problems the system of equations becomes nonlinear due to the electrostatic interactions between the dispersive fluxes of different charged species. Therefore, we use an iterative scheme with a Picard loop to linearize the coupled non-linear set of equations in each temporal step. The detailed computational steps for the multicomponent transport and reaction calculations are summarized in Table 1.

For each time step, *dt*, we consider the concentration vector from the advection step (i.e., after the advective shift of concentration) as an initial guess of the Picard iteration to determine the cross-coupled dispersion coefficients (Eqs. 9-10). Afterwards, we determine the mobility matrix $\mathbf{M}_{\mathrm{MOB},i}^{\mathrm{disp}}$ which results from the spatial discretization on streamline-oriented grids and contains the divergence of dispersive fluxes defined by the finite volume method (*Step 2*). The newly computed $\mathbf{D}_{ij}^{L}, \mathbf{D}_{ij}^{T}$ and $\mathbf{M}_{\mathrm{MOB},i}^{\mathrm{disp}}$ are then used to calculate the new concentration vector, $\boldsymbol{C}_{i}^{\mathrm{disp}}$ (*Step 3*). Here, $\mathbf{M}_{\mathrm{STORE},i}$ denotes the storage matrix resulting from the spatial discretization and describes the discrete cell-area

of each cell of the domain. $\boldsymbol{C}_i^{\text{adv}}$ represents the concentration vector after the advection step. At each time step, the iteration in the dispersion step repeats until the concentration vector reaches a constant value: i.e., when the norm of the differences among the concentration values in two consecutive iterations (κ and κ+1) converges to a very small user-defined threshold value (ε).

Table 1: Algorithm for transient multicomponent ionic transport and reaction computation.

Discretization:

$$\frac{\partial C_i}{\partial t} + \boldsymbol{v}\cdot\nabla C_i - \nabla\cdot\left(\sum_{j=1}^{N}\mathbf{D}_{ij}\nabla C_j\right) \Rightarrow \mathbf{M}_{\text{STORE},i}\frac{\partial \boldsymbol{C}_i}{\partial t} + \mathbf{M}_{\text{MOB},i}^{\text{adv}}\boldsymbol{C}_i + \mathbf{M}_{\text{MOB},i}^{\text{disp}}\boldsymbol{C}_i$$

Advection step:

$$\boldsymbol{C}_i^{\text{adv},t+dt} = \boldsymbol{C}_i^{t} + \left(\mathbf{M}_{\text{STORE},i}/dt\right)^{-1}\left(-\mathbf{M}_{\text{MOB},i}^{\text{adv},\kappa}\boldsymbol{C}_i^{t} + \boldsymbol{b}_i\right)$$

Dispersion step:

while $\text{norm}\left(\boldsymbol{C}_i^{\text{disp},t+dt(\kappa+1)} - \boldsymbol{C}_i^{\text{disp},t+dt(\kappa)}\right) > \varepsilon$

Step 1: Calculate the cross-coupled dispersion coefficients in each cell,

$$\mathbf{D}_{ij}^{L,t+dt(\kappa)} = \delta_{ij}D_{ij}^{L} - \frac{z_i z_j D_i^L D_j^L C_i^{\text{disp},t+dt(\kappa)}}{\sum_{k=1}^{N}\left(z_k^2 D_k^L C_k^{\text{disp},t+dt(\kappa)}\right)}$$

$$\mathbf{D}_{ij}^{T,t+dt(\kappa)} = \delta_{ij}D_{ij}^{T} - \frac{z_i z_j D_i^T D_j^T C_i^{\text{disp},t+dt(\kappa)}}{\sum_{k=1}^{N}\left(z_k^2 D_k^T C_k^{\text{disp},t+dt(\kappa)}\right)}$$

Step 2: Calculate mobility matrix for dispersion problem, $\mathbf{M}_{\text{MOB},i}^{\text{disp},t+dt(\kappa)}$

Step 3: Solve for the concentration,

$$\boldsymbol{C}_i^{\text{disp},t+dt(\kappa)} = \left(\mathbf{M}_{\text{STORE},i}/dt + \mathbf{M}_{\text{MOB},i}^{\text{disp},t+dt(\kappa)}\right)^{-1}\left(\mathbf{M}_{\text{STORE},i}\boldsymbol{C}_i^{\text{adv},t+dt}/dt\right)$$

Step 4: Next iteration: $\kappa = \kappa + 1$

end

Reaction step:

$$\boldsymbol{C}_i^{\text{disp},t+dt} \rightarrow \left[\textbf{PHREEQC}\right] \rightarrow \boldsymbol{C}_i^{\text{reac},t+dt}$$

3.2 Reaction Calculations and IPhreeqc Coupling

After the advection and dispersion steps, we perform reaction calculations with PHREEQC-3 [18] by using the IPhreeqc module [15]. In our calculations, we use the COM (component object model) version of IPhreeqc which allows all reaction capabilities of PHREEQC to be used by any software and scripting language that can interface with a Microsoft COM server, e.g., Excel®, Visual Basic®, Python, or MATLAB® [14,15]. After updating the species concentration within the transport step, the concentration vector is sequentially passed to IPhreeqc for reaction calculations. In the reaction step, the simulation is performed by considering a batch reactor in each cell of the 2-D model domain that contains user-defined physical and chemical properties representing the reactive processes of interest. After the reaction calculations, the newly updated concentration values in each cell are passed back to the transport model. Besides all dissolved species, the transport calculations also include elemental oxygen (O), hydrogen (H) and charge imbalance (CB) as extra solution components. These parameters allow PHREEQC recognizing the liquid phase (water) and tracking the charge balance which is important in various geochemical calculations [19] as well as for multicomponent ionic transport.

The formulation described above allows performing multicomponent ionic transport calculations in a rigorous way that collectively includes both the electrostatic coupling of dispersive fluxes and the full aqueous speciation computed by PHREEQC.

4. BENCHMARK PROBLEMS

The proposed multicomponent reactive transport model is benchmarked by comparing the model outcomes with: (a) the analytical solution of a 2-D transport problem, (b) a

high-resolution experimental dataset, (c) a classical 1-D ion-exchange problem solved with PHREEQC-3 and (d) 1-D ion exchange considering multicomponent ionic transport. For the sake of brevity we present in the following sections the benchmark cases (a) and (d), whereas the examples (b) and (c) can be found in the Supplementary Material.

4.1 Benchmark of Transient Multicomponent Ionic Transport

In order to test the performance of our transient multicomponent ionic transport code in a two-dimensional flow-through domain, we compare the simulation outcomes with an analytical solution of the classical 2-D advection-dispersion equation:

$$\frac{\partial C}{\partial t} = -v\frac{\partial C}{\partial x} + D_L\frac{\partial^2 C}{\partial x^2} + D_T\frac{\partial^2 C}{\partial z^2} \tag{13}$$

The analytical solution of the advection-dispersion equation in a semi-infinite two-dimensional perfectly homogeneous domain ($0<x<\infty$ and $-\infty<z<\infty$), considering transient transport of a solute initially distributed in a rectangular region with zero influx of solute mass at the upstream boundary (Eqs. 15-18), is given by [72,73]:

$$\begin{aligned} C(x,z,t) = \frac{C_0}{4}\Bigg[&\operatorname{erfc}\left(\frac{x-x_2-vt}{\sqrt{4D_i^L t}}\right) - \operatorname{erfc}\left(\frac{x-x_1-vt}{\sqrt{4D_i^L t}}\right) \\ &+ \exp\left(\frac{vx}{D_i^L}\right)\left\{\operatorname{erfc}\left(\frac{x+x_2+vt}{\sqrt{4D_i^L t}}\right) - \operatorname{erfc}\left(\frac{x+x_1+vt}{\sqrt{4D_i^L t}}\right)\right\}\Bigg] \cdot \left[\operatorname{erfc}\left(\frac{z-a}{2\sqrt{D_i^T t}}\right) - \operatorname{erfc}\left(\frac{z+a}{2\sqrt{D_i^T t}}\right)\right] \end{aligned} \tag{14}$$

The initial and boundary conditions are defined as:

$$C(x,z,0)=\begin{cases} C_0 & x_1 < x < x_2 \quad \text{and} \quad -a < z < a \\ 0 & \text{otherwise} \end{cases} \tag{15}$$

$$vC\big|_{x=0^+} = 0 \tag{16}$$

$$\frac{\partial C}{\partial x}(\infty, z, t) = 0 \tag{17}$$

$$\frac{\partial C}{\partial z}(x, \pm\infty, t) = 0 \tag{18}$$

where x_1 and x_2 are the longitudinal positions delimiting the initial location of the solute source. In the transverse direction, the solute is initially located between $-a$ and a.

We consider a two-dimensional homogeneous domain of 100 cm × 12 cm, which is discretized into 100 (Δx = 1 cm) and 240 (Δz = 0.5 mm) cells along the longitudinal and transverse dimension, respectively. The transport simulations are run for a total simulation time of t = 18 hours with a uniform horizontal velocity of v = 1.0 m/day. The porosity of the flow-through system is 0.41. We consider a rectangular solute source, with dimensions of 2 cm × 2 cm, initially located 2 cm downstream of the inlet boundary, between 5 and 7 cm along the vertical dimension (Fig. 2).

The simulation is performed for the transport of a single 1:1 electrolyte (NaCl) in pure ambient water. In such ionic systems, the electrostatic interactions couple the movement of the cation (Na^+) and the anion (Cl^-) and lead to an identical displacement of the two species. As a result, although the strong electrolyte (NaCl) fully ionizes in the aqueous solution and the two ions (Na^+ and Cl^-) are characterized by different mobility, they

travel as a single species in order to maintain electroneutrality. Hence, for this particular case, the diffusion (and dispersion) of these two ions can be characterized by a single diffusion coefficient (e.g., [36]):

$$D_{NaCl} = \frac{\left|z_{Na^+}\right| + \left|z_{Cl^-}\right|}{\left|z_{Na^+}\right| / D_{Cl^-}^{aq} + \left|z_{Cl^-}\right| / D_{Na^+}^{aq}} \tag{19}$$

where D_{NaCl} represents the combined diffusion coefficient of the electrolyte. z_{Na^+}, z_{Cl^-} and $D_{H^+}^{aq}$, $D_{Cl^-}^{aq}$ are the charge and the aqueous diffusion coefficients of Na^+ and Cl^-, respectively. Self-diffusion coefficients of sodium and chloride as well as of other ions used in the following sections are reported in Table 2. The value obtained combining diffusion coefficients of Na^+ and Cl^- (Eq. 19) for the salt is $D_{NaCl} = 1.44 \times 10^{-9}$ m^2/s. Therefore, the electrostatic ionic interactions reduce the multicomponent ionic transport problem into a single-species conservative transport problem. Thus, for this special case, the outcomes of the 2-D transient multicomponent ionic transport model can be directly compared with the results of the analytical solution (Eq. 14). In order to simulate transport in flow-through systems the hydrodynamic dispersion coefficients (Eq. 11) are calculated using the combined salt diffusion coefficient (Eq. 19) for the analytical solution (Eq. 14) and the self-diffusion coefficients of the individual ions for the numerical model. The latter takes into account the electrostatic interactions between Na^+ and Cl^- in the pore water by coupling their dispersive fluxes as explained in Section 2 and Section 3.

The comparison between the multicomponent ionic transport model and the analytical solution at the end of t = 18 hours of simulation is shown in Fig. 2. The instantaneous

303 rectangular slug source spreads and approaches a Gaussian elliptical shape during the
304 transport through the homogeneous porous medium (Fig. 2a-c). It is evident from the
305 two-dimensional concentration distributions that the concentrations both from the
306 multicomponent ionic transport simulations (Fig. 2a-b) and from the analytical solution
307 (Eq. 14, Fig. 2c) are very similar. Fig. 2 also shows the longitudinal (panel d) and
308 transverse (panel e) concentration profiles along the longitudinal and transverse axes
309 through the center of the plume. The coupled displacement of the Na^+ and Cl^- ions results
310 in overlapping concentration of these species both in the longitudinal and in the
311 transverse direction. These profiles perfectly match with the concentration profiles of the
312 combined electrolyte (i.e., NaCl salt as a single uncharged species) computed with the
313 analytical solution. Thus, these results validate the accuracy of the transient
314 multicomponent ionic transport simulations in conservative two-dimensional systems.

315 **Table 2:** Aqueous diffusion coefficients of different ions.

Diffusion coefficients	D^{aq} [m^2/s][a]
H^+	8.65×10^{-9}
Mg^{2+}	0.63×10^{-9}
Cl^-	1.81×10^{-9}
Na^+	1.20×10^{-9}
Br^-	1.86×10^{-9}
K^+	1.77×10^{-9}
Ca^{2+}	0.71×10^{-9}
NO_3^-	1.70×10^{-9}

[a] values from Lasaga [74], corrected for temperature and viscosity changes at 20°C

316

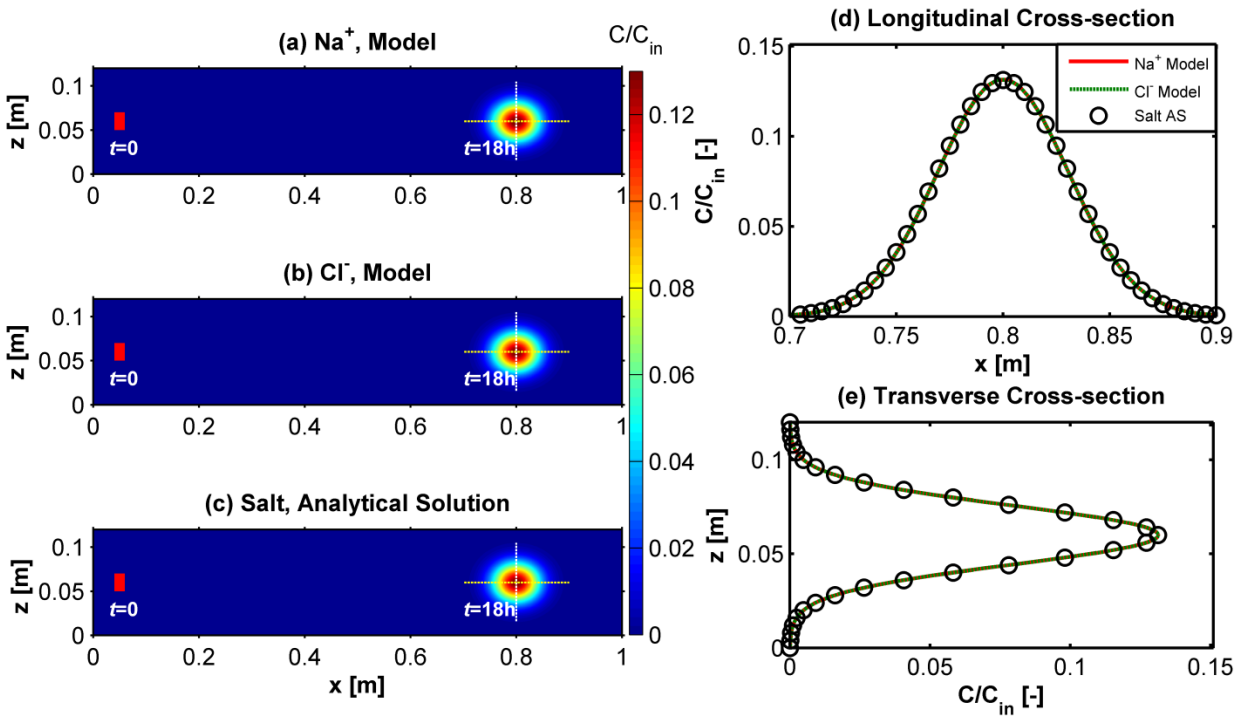

Figure 2: Comparison of the multicomponent ionic transport model and 2-D analytical solution for the transport of NaCl in pure water at v = 1 m/day: 2-D concentration distributions after t = 18 hours (a-c); longitudinal cross sectional profiles at z = 6 cm (d); transverse cross sectional profiles at x = 80 cm (e).

4.2 Benchmark of IPhreeqc Coupling: Ion-Exchange with Multicomponent Ionic Transport and Charge Interactions

In order to validate the coupling of our transport code with the geochemical code PHREEQC, we consider the example problem 11 of the PHREEQC-3 manual [18]. This example includes the advective-dispersive transport of ionic species in a one-dimensional, 8 cm long column containing a cation exchanger. The exchanger column, initially in equilibrium with a solution containing Na^+, K^+ and NO_3^-, is continuously flushed with a $CaCl_2$ solution. As a consequence, the cations (Na^+, K^+ and Ca^{2+}) undergo ion-exchange reactions with the exchanger and new equilibrium compositions of the exchanger and the pore water are established. The comparison between the 1D

PHREEQC simulation and the 2D simulation carried out with the proposed code is presented in the Supplementary Material. The ion-exchange problem was also extended to the case of transient multicomponent ionic transport. In this example, we specifically focus on multicomponent diffusion (with charge effects) and ion-exchange problem. In order to focus on the multicomponent effects, we consider diffusion-dominated transport in the virtual column setup, by decreasing of a factor of ten the value of the seepage velocity (v = 0.024 m/day). The column geometry, the exchanger properties and the involved ions and concentrations are kept the same as in the original example described above. Instead of a single diffusion coefficient for all ionic species, species-specific aqueous diffusion coefficients are used for different ions. The self-diffusion coefficients used for different species are reported in Table 2. For the sake of simplicity, dispersivity is neglected and thus is set to zero and the pore diffusion coefficients are assumed to be identical to the aqueous diffusion coefficients (i.e., porosity, θ = 1). The 1-D PHREEQC simulations are conducted by using the keyword **multi_d**, which allows accounting for multicomponent ionic transport [29]. On the other hand, in our two-dimensional transport code coupled with PHREEQC, multicomponent ionic transport calculations are performed by solving Eqs. (7-10) as illustrated in Section 3 and Table 1. Fig. 3 represents the simulated effluent breakthrough curves of different ionic species. Notice that, due to a smaller advective velocity, diffusion becomes more dominant in this case compared to the advection-dominated ion-exchange problem (Fig. S5, Supplementary Material). This is reflected in the smoother temporal concentration profiles of the ionic species. The evolution of Cl^- front shows an interesting pattern, with a sudden increase of Cl^- concentration, after ~1.75 PV when Ca^{2+} breakthrough starts. Such behavior is due to the

multicomponent ionic transport through the exchanger column and the requirement of maintaining charge balance throughout the domain. Furthermore, the two simulations, using PHREEQC alone in a 1-D domain and using the 2-D multicomponent ionic transport code combined with PHREEQC in a uniform 2-D domain (equivalent to 1-D), have the same outcome which, therefore, validates the transient multicomponent ionic transport calculations coupled with chemical reactions.

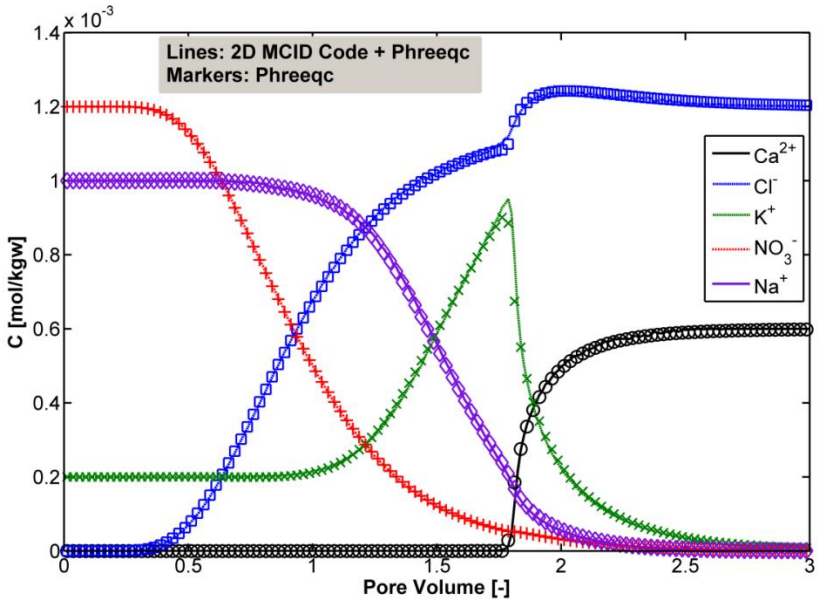

Figure 3: Benchmark of IPhreeqc coupling with the 2-D transport code for an example of ion-exchange coupled to multicomponent ionic transport with electrochemical migration.

5. EXAMPLES OF MULTICOMPONENT IONIC TRANSPORT SIMULATIONS

In this section we present scenarios of multicomponent transport of ionic solutes in both homogeneous and heterogeneous domains. Section 5.1 focuses on conservative multicomponent transport of electrolyte systems. The impact of charge effects on breakthrough curves and plume dilution of the different ionic species during conservative

transport are analyzed. Section 5.2 illustrates multicomponent transport of charged species undergoing ion-exchange reactions. We present scenarios with increasing level of complexity in terms of physical heterogeneity (i.e., spatially variable hydraulic conductivity) and chemical heterogeneity (i.e., spatially variable ion-exchange capacity).

5.1 Conservative Transport

5.1.1 Simulations in Homogeneous Domain

The simulations were performed to show the influence of charge interactions on transient multicomponent ionic transport. We consider two different domains, a homogeneous porous medium and a heterogeneous formation, at two different scales. For the homogeneous case, we select a 2-D domain with dimensions of 100 cm × 20 cm (L × W), similar to the laboratory setup recently used to investigate multicomponent ionic transport [37-39], and with a uniform distribution of hydraulic conductivity and flow-velocity. Such simulation domain is representative of typical laboratory bench-scale quasi two-dimensional flow-through chambers packed with uniform grain sized material (e.g., [39,43,75]). The simulations were run, by considering a rectangular slug of electrolytes as initial condition, at two different horizontal flow velocities of 0.1 m/day and 1.0 m/day. At each flow velocity, three different combinations of electrolyte scenarios are considered: (i) transport of a single electrolyte (HCl) in pure water; (ii) transport of a single electrolyte (HCl) in a background electrolyte solution (NaBr); and (iii) transport of mixed electrolytes (H^+, Mg^{2+} and Cl^-) in pure water. The selection of this particular set of electrolytes is based on the variability of their aqueous diffusion coefficients (Table 2) and demonstrates the multicomponent charge coupling effects on ions undergoing conservative transport. The geometry, hydraulic and transport properties of different

394 simulation domains are summarized in Table 3. It should be noted that these simulations
395 are run by considering the assumption that the transported ionic species do not interact
396 with the solid matrix and perfect conservative conditions exist.

397 Fig. 4 summarizes the breakthrough curves and transient flux-related dilution index for
398 different electrolyte cases at the outlet end of the homogeneous meter-scale domain. The
399 flux-related dilution index is a metric of mixing, originally developed for steady-state
400 plumes [76], that expresses dilution as the act of distributing a given solute mass flux
401 over a larger water flux and determines an effective volumetric discharge transporting the
402 solute flux at a given longitudinal cross section. For the transient multicomponent
403 transport of ionic species in flow-through domains, the flux-related dilution index of an
404 ion "*i*" can be defined as [77]:

$$E_{Q,i}(x,t) = \exp\left(-\int_{\Omega} p_{Q,i}(x,t) \ln p_{Q,i}(x,t) q_x(x,t) d\Omega \right) \tag{20}$$

405 where $q_x = v\theta$ is the longitudinal component of specific discharge, Ω is the cross-
406 sectional area, θ is the porosity, and $p_{Q,i}$ is the flux-related probability density function of
407 the charged species "*i*" at time *t*:

$$p_{Q,i}(x,t) = \frac{C_i(x,t)}{\int_{\Omega} C_i(x,t) q_x(x,t)} \tag{21}$$

408 The simulation outcomes at velocity of 0.1 m/day and 1 m/day are shown in Figs. 4a-f
409 and 4g-l, respectively. For the transport of a single electrolyte (HCl) in pure water,
410 despite having very different diffusivities (Table 2), the breakthrough curves of the cation
411 (H^+) and anion (Cl^-) are identical at both flow velocities (Fig. 4a and 4g). On the other

412 hand, during transport in the presence of a background electrolyte, their breakthrough
413 profiles are significantly different, with the faster ion (H^+) having more spread profiles
414 and lower peak concentrations compared to the slower one (Cl^-) (Fig. 4b and 4h). The
415 profiles of flux-related dilution index show identical values for transport in pure water
416 (Fig. 4d and 4j); whereas in the case of background electrolyte the cation (H^+) plume is
417 considerably more diluted (approximately 2 times) than the anion (Cl^-) plume (Fig. 4e
418 and 4k). This behavior is induced by the charge interactions between positively and
419 negatively charged species. During transport in pure water the cation and anion travel
420 together in order to fulfill the local charge balance and thus they are electrostatically
421 coupled. On the other hand, when the same ions are transported through a background
422 electrolyte solution, the domain is locally charge balanced by the background ions and,
423 consequently, the cation and anion in the solute plume can travel and subsequently dilute
424 according to their self-diffusive/dispersive properties. However, in both cases the $E_{Q,i}$
425 profiles for different ions show a monotonic increase over time at the outlet cross-section
426 of the domain (Fig. 4e and 4f).

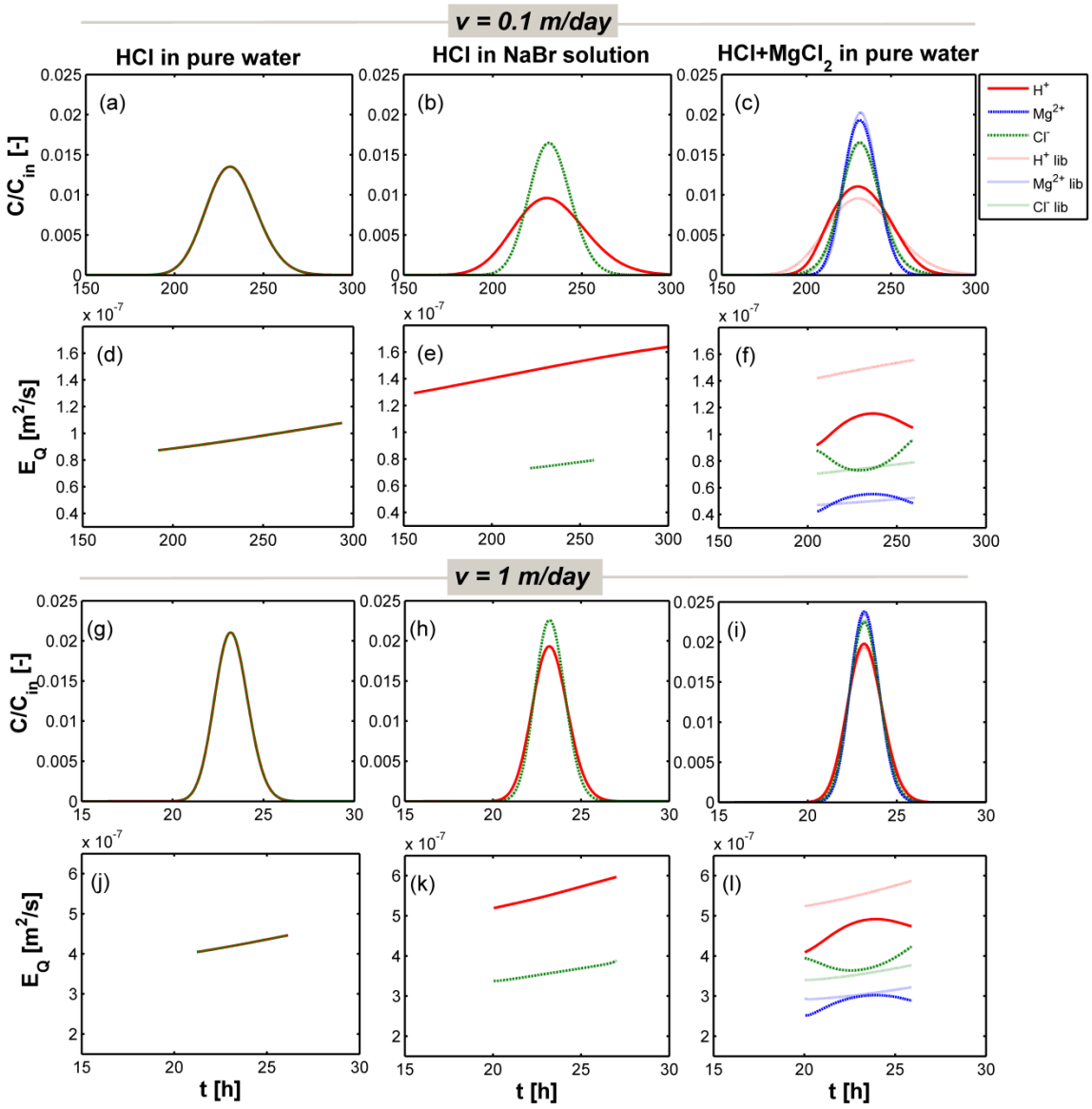

Figure 4: Breakthrough curves (a-c and g-i) and flux-related dilution indices (d-f and j-l) for simulations at v = 0.1 m/day (a-f) and v = 1 m/day 1 (g-l) in a homogeneous domain. $E_{Q,i}$ values are calculated for a concentration threshold equal to 10^{-6} of the peak concentration for each species.

For the transport of mixed electrolytes in pure water (H^+, Mg^{2+} and Cl^-), the breakthrough curves show a distinct pattern which follows the same order as suggested by their self-diffusivities (Table 2): where H^+ has the most spread profile with the lowest peak concentration and Mg^{2+} shows the least spread profile and the highest peak concentration (Fig. 4c). The Cl^- profile lies in between those of the cations. Due to the electrostatic

interaction during the displacement of the different ions, the profiles are also different compared to those of transport under "liberated" conditions (i.e., when they are transported as uncharged species). The behavior of the flux-related dilution index profiles of the ionic species for this scenario is quite interesting. The cation dilution profiles show a bulge-shape resembling a concave function. The cations have an increasing pattern of dilution reaching a maximum, and afterwards decreasing again (red and blue solid lines; Fig. 4f). The pattern is opposite (convex shaped) for the anion (Cl^-) for which the E_Q profile decreases and reaches a minimum at around mean breakthrough time and afterwards it starts increasing again (green lines; Fig. 4f). Such dilution behavior is significantly different compared to the monotonic increase at their "liberated" state (dotted lines; Fig. 4f) and can be explained considering the ionic interactions between the transported species. In fact, at early breakthrough times, when the fringe of the plume arrives at the outlet boundary, H^+ is more enriched compared to Mg^{2+} because of the higher diffusive/dispersive properties of H^+. As a consequence, H^+ is mainly responsible for counterbalancing the negative charge of Cl^- in the fringe area. Therefore, at the edge of the plume, the dilution of H^+ and Cl^- are similar, as reflected in their very early and late time $E_{Q,i}$ values, and these ions tend to be electrostatically coupled. Thus, among these two abundant species in the fringe zone, the diffusivity of H^+ decreases and the one of Cl^- increases compared to their true "liberated states" in order to maintain charge balance. On the other hand, in the center of the plume, Mg^{2+} has a higher relative concentration and hence higher contribution to counter the negative charge of Cl^-. So, in this case, E_{Q,Cl^-} decreases due to a stronger coupling to a slower positive ion (Mg^{2+}), and for the same reason Mg^{2+} dilution increases compared to its liberated values (Fig. 4f).

460 The differences between the actual dilution of the ions' plumes compared to their
461 theoretical displacements at "liberated state" are notable for all the reported ions, as
462 shown by the different patterns of the corresponding lines in Fig. 4f.

463 Similar patterns of concentration and dilution breakthrough curves are obtained at higher
464 velocity (v = 1 m/day) (Figs. 4g-l). Due to the advection-dominated transport,
465 breakthrough curves are less spread (narrow profiles with higher peak concentrations)
466 compared to their respective cases at slow velocity (v = 0.1 m/day). Interestingly, because
467 of the higher Péclet numbers (i.e., higher values of dispersion coefficients) at v = 1 m/day
468 the absolute values of dilution indices ($E_{Q,i}$) are considerably higher (approximately 5
469 times) with respect to the ones obtained at slow velocity (Figs. 4j-l, 4d-f). This implies
470 that, even though the breakthrough curves and the concentration distribution are less
471 spread, the plumes are in fact more diluted at higher seepage velocity, since the mass
472 fluxes of the different ions are distributed over larger water fluxes.

473 *5.1.2 Simulations in Heterogeneous Domain*

474 The analogous set of simulations was also performed in a heterogeneous domain to
475 investigate the large-scale effects and the influence of heterogeneity on breakthrough and
476 dilution during conservative multicomponent ionic transport. The simulations were run in
477 a randomly generated two-dimensional flow-field (20 m × 2.5 m) representing a vertical
478 cross-section of a mildly heterogeneous aquifer. The hydraulic conductivity statistics are
479 consistent with those reported for the Borden aquifer [78] and the mean hydraulic
480 gradient was adjusted to produce average flow velocities of 0.1 and 1 m/day. The domain
481 is discretized into 200 cells (Δx = 10 cm) in the horizontal direction and 250 cells (Δz = 1
482 cm) in the vertical direction. The heterogeneous conductivity field is generated with an

exponential covariance model and by using the spectral approach described by Dykaar and Kitanidis [79]. The summary of hydraulic and transport parameters used in the simulations are given in Table 3.

Table 3. Summary of geometry, flow and transport parameters of the homogeneous and heterogeneous domains.

Parameters	**Homogeneous**[a]	**Heterogeneous**[b]
Domain size (L×H) [m]	1 × 0.2	20 × 2.5
Discretization, $\Delta x/\Delta z$ [cm]	0.5/0.1	10/1
Slug size [m]	0.02 × 0.02	0.4 × 0.2
Average hydraulic conductivity [m/s]	1.27×10^{-2}	9.75×10^{-5}
$\sigma^2_{\ln K}$	-	0.29
Average horizontal flow velocity [m/day]	0.1; 1	0.1; 1
Average porosity [-]	0.41	0.34

[a]Data consistent with the experimental setup of Rolle et al. [37]
[b]Data consistent with the characterization of the Borden aquifer (Sudicky [78])

Fig. 5 shows the results of conservative transport simulation of mixed electrolytes in the generated 2-D random fields for an average flow velocity of 1 m/day, using spatially-variable local hydrodynamic dispersion coefficients in which the mechanical dispersion term is linked to the hydraulic conductivity through the average grain size (Eq. 12). The simulated velocities and streamlines are shown in Fig. 5a. The concentration distribution of the plume containing mixed electrolytes (HCl and $MgCl_2$) after 7 days of simulation is depicted in Fig. 5b-d. It is evident that due to heterogeneity and flow variability, the shapes of the different ionic plumes are irregular. It is interesting to notice that even in this spatially variable domain and under an advection-dominated regime (average v = 1 m/day), the compound-specific behavior of the different ions is still significant as shown by the different distributions of the two cations and of the anion concentration. Due to a higher diffusivive/dispersive properties, the H^+ plume is evidently more diluted and

shows a lower peak concentration compared to the other two ions (Fig. 5b). On the other hand, the Mg^{2+} plume is more affected by the spatial variability of the velocity distribution and consequently results in a more stretched but less diluted plume with a higher peak concentration (Fig. 5c). The shape of the anion (Cl^-) plume appears to be in-between those of the cations.

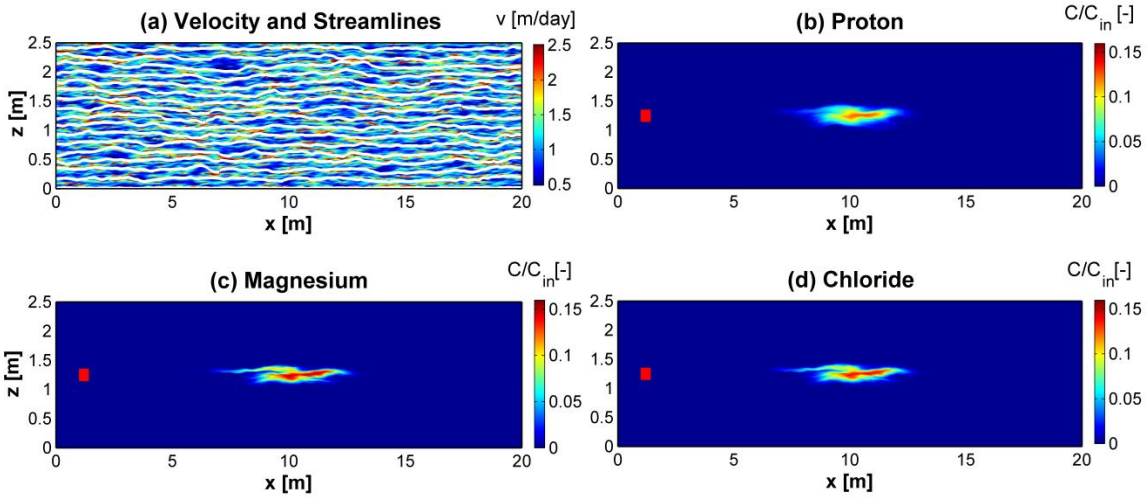

Figure 5: Seepage velocity distribution and streamlines (a); 2-D concentration maps (b-d) for mixed electrolyte case at v = 1 m/day after t = 7 days. The red rectangle represents the initial location of the solute slug (b-d).

The breakthrough curves of concentration and flux-related dilution index ($E_{Q,i}$), at the end of the domain, are illustrated in Fig. 6 for different simulations. Although the shape of the 2-D concentration distribution for different ions looks very irregular (non-Gaussian; Figs. 5b-d), their depth-integrated breakthrough curves have almost regular shape (Figs. 6a-c, g-i) in this mildly-heterogeneous domain.

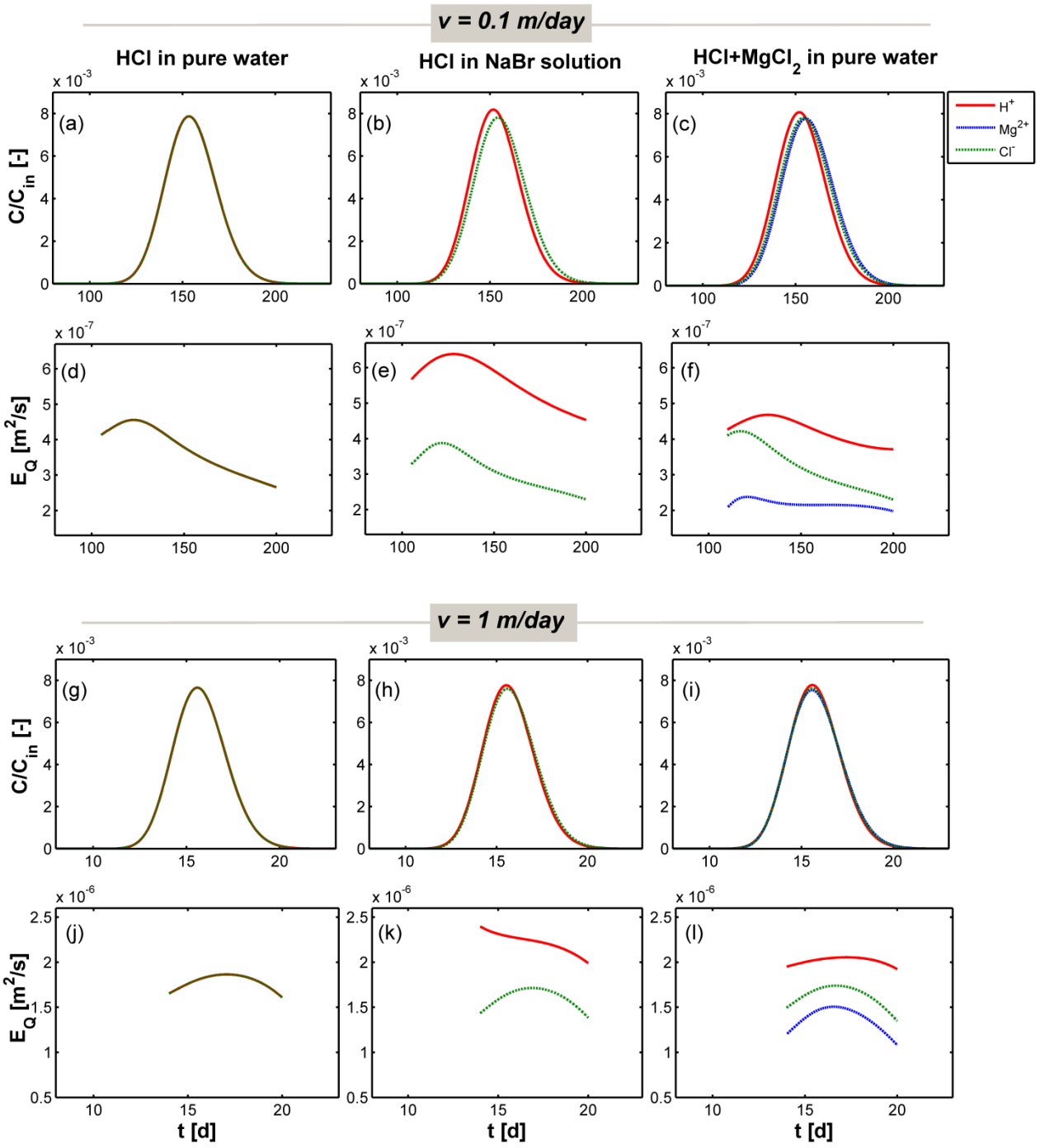

515

516 **Figure 6:** Breakthrough curves (a-c and g-i) and flux-related dilution indices (d-f and j-l)
517 for simulations at v = 0.1 m/day (a-f) and 1 m/day (g-l) in a heterogeneous domain. $E_{Q,i}$
518 values are calculated for a concentration threshold equal to 10^{-6} of the peak concentration
519 for each species.

520

For the transport of both HCl in a background electrolyte (Fig. 6b,h) as well as for the case of mixed electrolyte in pure water (Fig. 6c,i), the differences among the ionic temporal profiles are smaller compared to those observed in homogeneous domain. However, the differences in dilution between the ions are still significant as shown by the computed trends of $E_{Q,i}$. Unlike the regular increase of $E_{Q,i}$ in the homogeneous domain, the dilution breakthroughs in the heterogeneous flow field have a non-monotonic pattern. As observed in pore-scale domains [77], also for these continuum simulations such behavior can be attributed to the spatial variability of the velocity field and mass transfer limitations in the low-permeability zones of the heterogeneous flow field. Despite the different and irregular shape of the dilution breakthroughs compared to a homogeneous domain, the computed values of $E_{Q,i}$ at both flow velocities show the clear and persistent effect of the electrostatic coupling also in the heterogeneous flow field. This important feature can also be clearly appreciated from the maps of the ion concentration distributions (Fig. 5) but would be missed if one were to analyze exclusively flux-averaged concentration breakthrough curves at the outlet of the domain (Fig. 6 a-c and g-i).

The effect of electrostatic coupling is also evident from the maps of the dispersive flux components. As an example, Fig. 7 shows the results of transverse dispersive fluxes for the case of mixed electrolytes at v = 0.1 m/day. It is interesting to notice the interplay between the pure dispersive and the electrochemical migration components. For instance, considering H^+ it can be clearly observed that the electromigration component can have both a positive and a negative contribution to the total dispersive flux (Fig. 7g). Thus, the displacement of the ion can be increased or decreased in different locations within the

plume. Similar considerations are valid for the other cation and for the anion. The latter shows an inversely correlated behavior with respect to H^+, with displacement of Cl^- ions enhanced in the plume fringe, where they are mostly coupled to H^+, and decreased in the plume core, where the charge interaction is stronger with Mg^{2+}. Mapping of the ionic flux components helps understanding and visualizing the coupling between the transport of charged species and confirms a similar behavior as noticed in the small scale homogeneous domain by analyzing the dilution breakthrough curves (Fig. 4f and 4l).

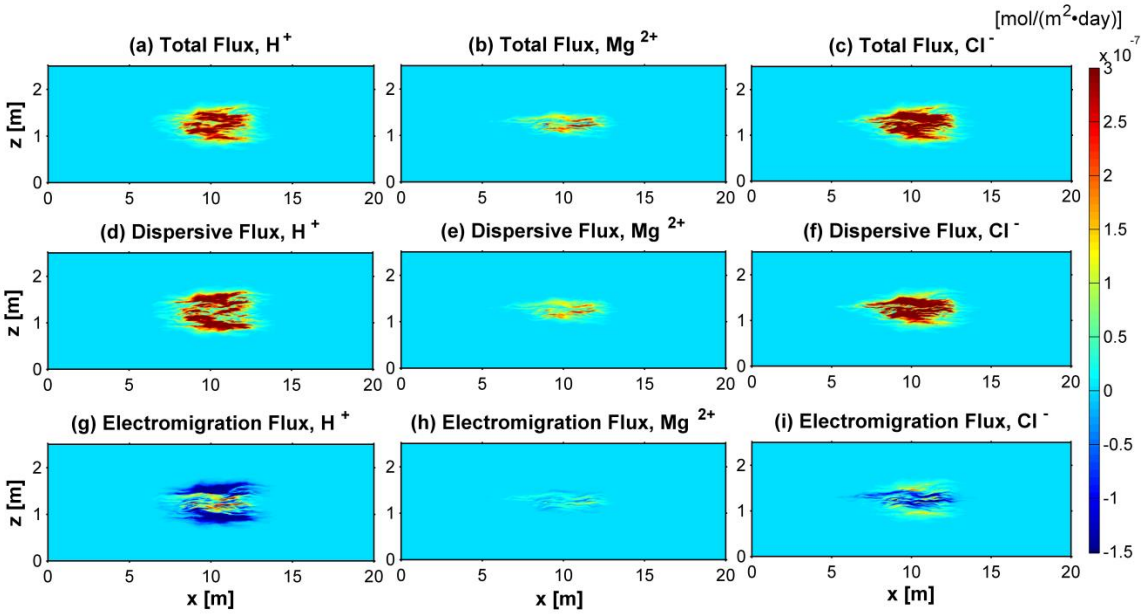

Figure 7: Maps of multicomponent ionic transverse fluxes for the transport of mixed electrolytes after 70 days (v = 0.1 m/day): Total fluxes (a, b, c), Dispersive fluxes (d, e, f) and Electrochemical migration fluxes (g, h, i). The direction from the core to the fringe of the plume is considered positive for the calculated fluxes.

5.2 Multicomponent Reactive Transport

In this section we present examples of two-dimensional multicomponent ionic transport coupled to chemical reactions in physically and chemically heterogeneous domains. We consider ion-exchange reactions and, similarly to a previous study [80], we extend a 1-D

example problem (Section 4.2) to two-dimensional spatially-variable domains. We focus on multicomponent ionic transport and we consider a slug release of $CaCl_2$ in a 2-D domain containing Na^+, K^+ and NO_3^- as initial and ambient solution. The simulations are run in heterogeneous domains with different distributions of key physical and chemical parameter such as the hydraulic conductivity and the cation exchange capacity (Table 4).

Table 4: Description of the multicomponent reactive transport scenarios.

Scenario	***K* distribution**	***CEC* distribution**	**Domain size**	**Slug size**
A	heterogeneous	homogeneous	20 m × 2.5 m	4 m × 0.3 m
B	heterogeneous	heterogeneous	20 m × 2.5 m	4 m × 0.3 m

The simulations were run in the randomly generated 2-D fields with the same geometry and hydraulic properties of those used in Section 5.1.2. Fig. 8 shows distributions of the controlling physical and chemical parameters. In both scenarios, we consider solute slugs of $CaCl_2$ (6 mM), initially placed 1 m downstream of the inflow boundary and with dimensions of 4 m × 0.3 m, that were transported through the heterogeneous domains. The inflow and initial solutions contain $NaNO_3$ (1 mM) and KNO_3 (0.2 mM).

Scenario A considers the effects of physical heterogeneity on the reactive transport problem. In this particular scenario, a uniform value of *CEC* (1.1 meq/L; same as [18]) was used throughout the entire physically heterogeneous domain.

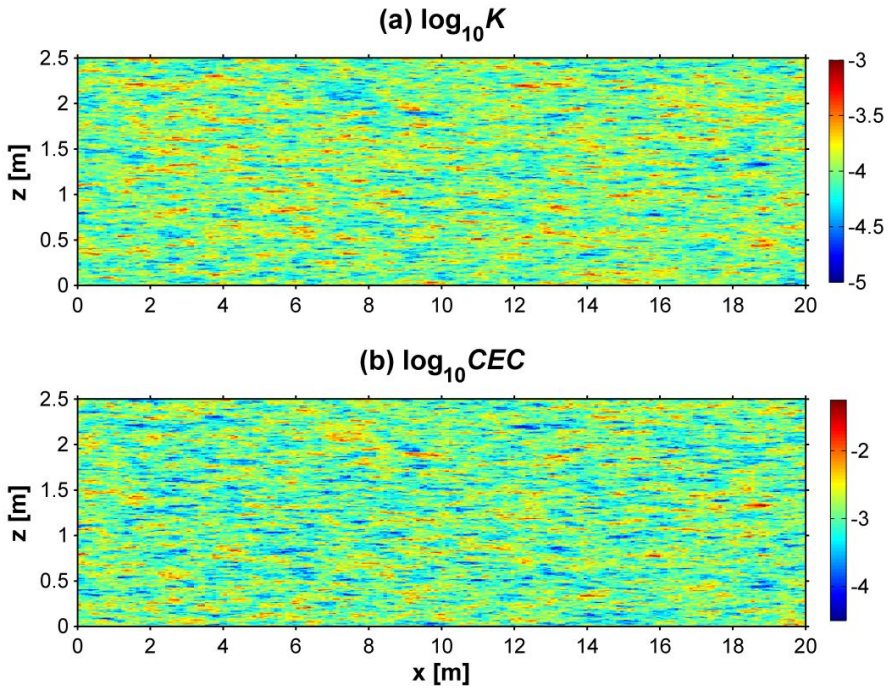

Figure 8: (a) Spatial distribution of hydraulic conductivity K (m/s) used in the simulated reactive transport scenarios A and B. (b) Spatial distribution of cation exchange capacity, CEC (eq/L) used in Scenario B.

In Scenario B, *CEC* values (Fig. 8b) were attributed to each cell of the domain considering a negative correlation with hydraulic conductivity as suggested in previous studies (e.g., [80-83]):

$$\ln CEC = a \ln K + b \tag{22}$$

where a and b are coefficients relating the hydraulic conductivity, K and the cation exchange capacity, *CEC*. In a field study, Christiansen et al. [81] identified a negative correlation between K and *CEC* in an aquifer (a = -0.59) composed of calcareous and non-calcareous layers. We base our simulations on the negative correlation proposed in that study, implying that the low-permeability regions have higher cation exchange capacity than the high-permeability zones (and vice versa).

589 Fig. 9 summarizes the results of the multicomponent reactive transport simulations
590 performed in scenarios A and B. The top row of panels depict the 2-D concentration
591 distribution of the cation plumes (Ca^{2+}; Fig. 9a,e) and the lower two rows of panels show
592 the distribution of the background cations (Na^{+} and K^{+}) after 75 days of simulation. All
593 simulations are run at an average seepage velocity of 0.1 m/day. Fig. 9a-c shows the
594 spatial distribution of different cations plumes in Scenario A. In this domain, the solute
595 slug $CaCl_2$ moves with groundwater along the 2-D random flow-field containing
596 homogeneous cation-exchange properties. All the ionic plumes show irregularities
597 because of the spatially variable hydraulic conductivity and velocity distributions. The
598 displacing cation, Ca^{2+}, shows a tailing in the upstream front and a sharper interface in
599 the downstream front of the plume. As it propagates through the domain, Ca^{2+} reacts with
600 the exchanger and displaces the background cations (K^{+} and Na^{+}) from the solid. Because
601 of different affinities towards the solid phase, a chromatographic sequence is clearly
602 observed among the positive ions: with Na^{+} (lowest affinity, Fig. 9c) being the first
603 species released from the solid phase, followed by K^{+} (Fig. 9b) and, finally, by the
604 displacing species Ca^{2+} (highest affinity, Fig. 9a).

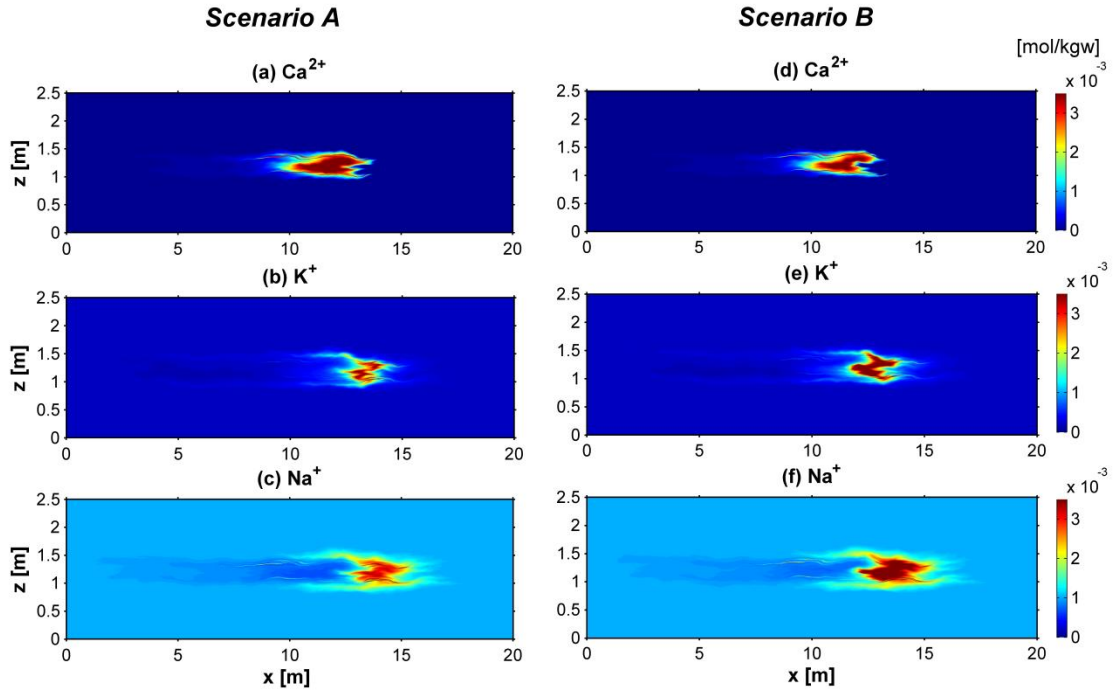

Figure 9: 2-D concentration distribution of cations in Scenario A (a-c) and B (d-f) after 75 days of simulation.

The effect of K^+ and Na^+ displacement from the solids is also reflected from the fact that these background cations show a surplus of dissolved concentration relative to their initial values (Fig. 9b-c). The center of mass of the cation plumes also moves with different apparent velocities: with Na^+ being the fastest species and Ca^{2+} being the slowest one.

In Scenario B, the solute slug migrates with groundwater along random flow paths and in a geochemically heterogeneous domain. The concentration and spreading of cation plumes (Fig. 9d-f) are quite different compared to the previous scenario. The background ions (K^+ and Na^+) contain relatively higher concentration in the dissolved phase compared to Scenario A (relative differences in the peak concentrations are ~32% for K^+ and ~11% for Na^+) . Conversely, Ca^{2+} shows a distribution that has smaller peak concentration (approximately 22%) relative to the plume in Scenario A (Fig. 9a,d). This

620 implies that the heterogeneous distribution of geochemical properties leads to an
621 enhancement of ion-exchange reactions and more effective retention of Ca^{2+}. After 75
622 days of simulation, the total mass of Ca^{2+} in the dissolved phase is ~34% smaller in the
623 chemically heterogeneous domain with respect to Scenario A. This behavior can also be
624 further confirmed from the depth-integrated breakthrough curves of Ca^{2+} at the end of the
625 heterogeneous domains (Fig. 10a). The depth-integrated peak concentration of Ca^{2+} in
626 Scenario B (red solid line) is significantly smaller (approximately ~5 times) compared to
627 Scenario A (black solid line). The mean arrival of breakthrough in Scenario B is also
628 considerably delayed (~20 days) compared to Scenario A. The dotted lines represent the
629 breakthrough curves of respective scenarios by ignoring the charge interactions (i.e., as
630 "liberated state"); while keeping the other hydraulic, transport and geochemical
631 conditions identical in the simulations. Scenario B is a random realization with the same
632 average CEC of scenario A. However, the total cation exchange capacity in the two
633 systems is different and this has an important effect on the breakthrough of calcium in the
634 two setups. Therefore, we considered an additional case in which not the average, but the
635 total CEC is the same in the two cases. The results of this additional simulation are
636 reported in Fig. 10b and show a closer behavior in terms of both arrival time and peak
637 concentration between scenario A and scenario B. It is interesting to notice that in all
638 cases a contribution due to electrochemical migration can be appreciated even in the
639 integrated profiles. Such contribution, in the considered physically and/or chemically
640 heterogeneous realizations, tends to cause an additional retardation of the calcium
641 plumes. We attribute this observation to the enhancement of Ca^{2+} dispersion fluxes
642 through the electrostatic coupling with the more mobile anions present in the domain.

643 This results in lower peak concentrations and more spread Ca^{2+} profiles. Such differences
644 in displacement do not only influence the breakthrough of calcium but also the mass
645 recovered at the outlet. In fact, the electromigration contribution to the dispersive fluxes
646 causes enhanced displacement of calcium at the outer fringe of the plume. In these
647 regions calcium comes into contact with solid with available CEC and, thus, it is retained
648 more effectively in the solid phase. As a consequence, a lower portion of the mass is
649 recovered at the outlet.

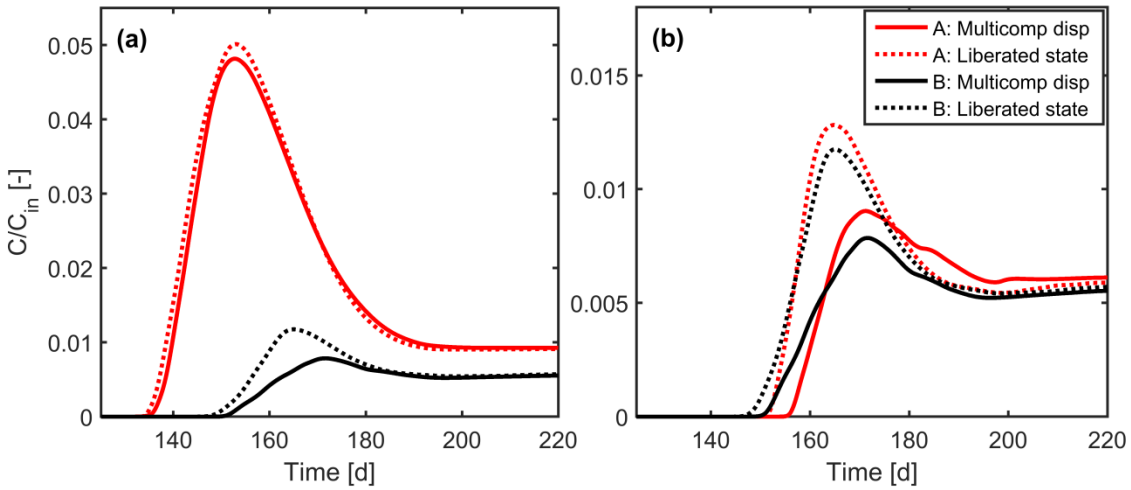

650
651 **Figure 10**: Depth-integrated breakthrough curves of Ca^{2+} at the end of the heterogeneous
652 domain in Scenario A and B, considering multicomponent ionic transport (solid lines) as
653 well as transport in "liberated" state (dotted lines). (a) Simulations with same average
654 CEC between Scenario A and B; (b) Simulations with same total CEC between Scenario
655 A and B.

656
657 **6. SUMMARY AND CONCLUSIONS**

658 In this paper, we presented a two-dimensional multicomponent reactive transport model
659 which is capable of taking into account the electrochemical migration effects during ionic
660 transport as well as a wide range of geochemical reactions. The modeling framework is
661 based on a multicomponent formulation of diffusive/dispersive fluxes and on the

662 compound-specific and spatially variable description of local hydrodynamic dispersion.
663 The proposed approach allows a detailed description of physical and electrochemical
664 processes during multicomponent ionic transport in both homogeneous and
665 heterogeneous formations. Additionally, the multicomponent ionic transport model is
666 coupled with the geochemical code PHREEQC, thus providing the flexibility of
667 simulating a wide variety geochemical reactions included in the PHREEQC package.
668 Two-dimensional conservative and reactive (ion-exchange) transport scenarios were
669 presented to demonstrate the capability of the developed model to simulate
670 multicomponent ionic transport in physically and chemically heterogeneous formations.
671 The simulations were performed in a homogeneous porous medium at laboratory scale, as
672 well as in heterogeneous porous media at the field scale. The simulation outcomes show
673 that the micro-scale physical (diffusion/dispersion) and/or electrochemical processes
674 (Coulombic interactions) significantly affect the macro-scale transport and dilution both
675 in the homogeneous and in the heterogeneous domains. For conservative transport, the
676 results of this study show that the coupling effects of charge interactions can be
677 appreciated from the 2-D distribution of the different ions and quantified using metrics of
678 mixing such as the flux-related dilution index. However, such effects might be
679 overlooked by only analyzing flux-averaged concentration breakthrough curves.
680 Furthermore, mapping the different components of the dispersive fluxes is also very
681 useful to understand and visualize the Coulombic coupling between the different ions and
682 the effects of electrochemical migration. The impact of electrostatic interactions is also
683 shown to be significant for the evolution of reactive plumes undergoing cation exchange
684 in physically and geochemically heterogeneous domains. For these scenarios we found

685 that the two-dimensional concentration distributions of the transported ions, as well as
686 their integrated breakthrough curves at the outlet, are affected by the electrochemical
687 migration terms coupling the transport of the charged species. Such effects influence the
688 displacement of the dissolved ions in the pore water as well as their interaction with the
689 solid matrix, since a different displacement compared to the "liberated state" causes the
690 ions to interact with different reactive zones of the porous medium.

691 Besides the specific scenarios investigated in this study, the proposed multicomponent
692 ionic transport code can be used to explore the effects of Coulombic interactions in
693 porous media in a wide variety of reactive transport problems. This can include mineral
694 precipitation and dissolution, sorption and surface complexation reactions, propagation of
695 pH fronts, mobilization of heavy metals and metalloids and biodegradation reactions
696 (e.g., [84-90]). We think that the code offers particular advantages for the study of
697 transport and Coulombic interactions in flow-through systems when the aim is to provide
698 a detailed description of the effects of physical and chemical heterogeneity. The current
699 model formulation is limited to multicomponent ionic transport of dilute solutions in two-
700 dimensional formations. Further work is required to extend the framework to systems
701 with strong gradients of ionic strength and to three-dimensional transport problems. For
702 fully 3-D transport, recent experimental studies have shown a more pronounced effect of
703 diffusion and compound-specific dispersion on solute displacement and plume dilution
704 [45]. Therefore, under these conditions, the effects of Coulombic interactions on the
705 displacement of charged species are expected to be more pronounced compared to two-
706 dimensional systems. Furthermore, in fully three-dimensional anisotropic heterogeneous
707 porous media, the topology of the flow field and the possible development of twisting

streamlines may play a major role on solute transport [91-93] and, thus, will also be of interest for multicomponent ionic transport problems.

Acknowledgments

This work was supported by the Baden-Württemberg Stiftung under the Eliteprogram for Postdocs. We would like to thank Prof. O. A. Cirpka (University of Tübingen) for discussion and for providing an early version of the streamline oriented code.

References

[1] Steefel CI, Appelo CAJ, Arora B, Jacques D, Kalbacher T, Kolditz O,Yeh GT. Reactive transport codes for subsurface environmental simulation. Computat Geosci 2015; 19:445-78. doi: 10.1007/s10596-014-9443-x.

[2] Barry DA, Prommer H, Miller CT, Engesgaard P, Brun A, Zheng C. Modelling the fate of oxidisable organic contaminants in groundwater. Adv Water Resour 2002;25: 945-83. doi: http://dx.doi.org/10.1016/S0309-1708(02)00044-1.

[3] Steefel CI, Lasaga AC. A coupled model for transport of multiple chemical-species and kinetic precipitation dissolution reactions with application to reactive flow in single-phase hydrothermal systems. Am Journal Sci 1994;294:529-92.

[4] Bethke C. Modelling transport in reacting geochemical systems. CR Acad Sci Ii A 1997;324:513-28.

[5] Prommer H, Barry DA, Zheng C. MODFLOW/MT3DMS-based reactive multicomponent transport modeling. Ground Water 2003, *41*, 247–257.

[6] Parkhurst DL, Kipp KL, Engesgaard P, Charlton SR. PHAST - A program for simulating ground-water flow, solute transport, and multicomponent geochemical reactions. Geochim Cosmochim Acta 2005; 69.

[7] Yeh GT, VS Tripathi. HYDROGEOCHEM: A coupled model HYDROlogical transport and GEOCHEMical equilibrium of multi component systems. ORNL 6371, Oak Ridge National Laboratory 1990.

[8] Xu T, Pruess K. Modeling multiphase non-isothermal fluid flow and reactive geochemical transport in variably saturated fractured rocks 1: Methodology. Am J Sci 2001;301:16-33, doi: 10.2475/ajs.301.1.16.

[9] Xu T, Sonnenthal E, Spycher N, Pruess K. TOUGHREACT—A simulation program for non-isothermal multiphase reactive geochemical transport in variably saturated geologic media: Applications to geothermal injectivity and CO2 geological sequestration. Comput Geosci 2006;32:145-65. doi: http://dx.doi.org/10.1016/j.cageo.2005.06.014.

[10] Xu T, Spycher N, Sonnenthal E, Zhang G, Zheng L, Pruess K. TOUGHREACT Version 2.0: A simulator for subsurface reactive transport under non-isothermal multiphase flow conditions. Comput Geosci 2011;37:763-74. doi: http://dx.doi.org/10.1016/j.cageo.2010.10.007.

[11] Mayer KU, Frind EO, Blowes DW. Multicomponent reactive transport modeling in variably saturated porous media using a generalized formulation for kinetically controlled reactions. Water Resour Res 2002;38:1301-21. doi: 10.1029/2001WR000862.
[12] Šimunek J, Jacques D, Šejna M, Van Genuchten MT. The HP2 program for HYDRUS (2D/3D): A coupled code for simulating two-dimensional variably-saturated water flow, heat transport, and biogeochemistry in porous media, Version 1.0. PC Progress, Prague, Czech Republic 2012:76.
[13] Mao X, Prommer H, Barry DA, Langevin CD, Panteleit B, Li L. Three-dimensional model for multi-component reactive transport with variable density groundwater flow. Environ Model Softw 2006;21:615-28. doi: http://dx.doi.org/10.1016/j.envsoft.2004.11.008.
[14] Wissmeier L, Barry DA. Implementation of variably saturated flow into PHREEQC for the simulation of biogeochemical reactions in the vadose zone. Environ Model Softw 2010;25:526-38. doi: http://dx.doi.org/10.1016/j.envsoft.2009.10.001.
[15] Charlton SR, Parkhurst DL. Modules based on the geochemical model PHREEQC for use in scripting and programming languages. Comput Geosci 2011;37:1653-63. doi: http://dx.doi.org/10.1016/j.cageo.2011.02.005.
[16] Parkhurst DL, Wissmeier L. PhreeqcRM: A reaction module for transport simulators based on the geochemical model PHREEQC. Adv Water Resour 2015;83:176-89. doi: http://dx.doi.org/10.1016/j.advwatres.2015.06.001.
[17] Parkhurst DL, Appelo CAJ. User's guide to PHREEQC (Version 2) - A computer program for speciation, batch-reaction, one-dimensional transport, and inverse geochemical calculations. U.S. Geological Survey Water Resources Investigations Report 1999; 99-4259.
[18] Parkhurst DL, Appelo CAJ. Description of input and examples for PHREEQC version 3- A computer program for speciation, batch-reaction, one dimensional transport, and inverse geochemical calculations. U.S. Geological Survey Techniques and Methods 2013;6-A43:497. available only at http://pubs.usgs.gov/tm/06/a43/.
[19] Wissmeier L, Barry DA. Simulation tool for variably saturated flow with comprehensive geochemical reactions in two- and three-dimensional domains. Environ Model Softw 2011;26:210-8. doi: http://dx.doi.org/10.1016/j.envsoft.2010.07.005.
[20] Müller M, Parkhurst DL, Charlton SR. Programming PHREEQC calculations with C++ and Python - A comparative study. In: Maxwell R, Poeter E, Hill M, Zheng C, MODFLOW and More 2011 - Integrated Hydrological Modeling Proceedings 2011:632-636.
[21] Nardi A, Idiart A, Trinchero P, de Vries LM, Molinero J. Interface COMSOL-PHREEQC (iCP), an efficient numerical framework for the solution of coupled multiphysics and geochemistry. Comput Geosci 2014;69:10-21. doi: http://dx.doi.org/10.1016/j.cageo.2014.04.011.
[22] Nasir O, Fall M, Evgin E. A simulator for modeling of porosity and permeability changes in near field sedimentary host rocks for nuclear waste under climate change influences. Tunn Undergr Sp Tech 2014;42:122-35. doi: http://dx.doi.org/10.1016/j.tust.2014.02.010.
[23] Kolditz O, Bauer S, Bilke L, Böttcher N, Delfs JO, Fischer T, Zehner B. OpenGeoSys: An open-source initiative for numerical simulation of thermo-hydro-

mechanical/chemical (THM/C) processes in porous media. Environ Earth Sci 2012;67:589-99. doi: 10.1007/s12665-012-1546-x.
[24] He W, Beyer C, Fleckenstein JH, Jang E, Kolditz O, Naumov D, Kalbacher T. A parallelization scheme to simulate reactive transport in the subsurface environment with OGS#IPhreeqc 5.5.7-3.1.2. Geosci Model Dev 2015;8:3333-48. doi: 10.5194/gmd-8-3333-2015.
[25] Korrani AKN, Sepehrnoori K, Delshad M. Coupling IPhreeqc with UTCHEM to model reactive flow and transport. Comput Geosci 2015;82:152-69, doi: http://dx.doi.org/10.1016/j.cageo.2015.06.004.
[26] Vinograd JR, McBain JW. Diffusion of electrolytes and of the ions in their mixtures. J Am Chem Soc 1941;63:2008-15. doi: 10.1021/ja01852a063.
[27] Liu CX, Shang JY, Zachara JM. Multispecies diffusion models: A study of uranyl species diffusion. Water Resour Res 2011; 47: W12514. http://dx.doi.org/10.1029/2011WR010575.
[28] Giambalvo ER, Steefel CI, Fisher AT, Rosenberg ND, Wheat CG. Effect of fluid-sediment reaction on hydrothermal fluxes of major elements, eastern flank of the Juan de Fuca Ridge. Geochim Cosmochim Acta 2002;66:1739-57. doi: 10.1016/S0016-7037(01)00878-X.
[29] Appelo CAJ, Wersin P. Multicomponent diffusion modeling in clay systems with application to the diffusion of tritium, iodide, and sodium in opalinus clay. Environ Sci Tech 2007;41:5002-7. doi: Doi 10.1021/Es0629256.
[30] Appelo CAJ, Vinsot A, Mettler S, Wechner S. Obtaining the porewater composition of a clay rock by modeling the in- and out-diffusion of anions and cations from an in-situ experiment. J Contam Hydrol 2008;101:67-76. doi: DOI 10.1016/j.jconhyd.2008.07.009.
[31] Appelo CAJ, Van Loon LR, Wersin P. Multicomponent diffusion of a suite of tracers (HTO, Cl, Br, I, Na, Sr, Cs) in a single sample of Opalinus Clay. Geochim Cosmochim Acta 2010;74:1201-19. doi: 10.1016/j.gca.2009.11.013.
[32] Ben-Yaakov S. Diffusion of sea water ions—I. Diffusion of sea water into a dilute solution. Geochim Cosmochim Acta 1972;36:1395-406. doi: 10.1016/0016-7037(72)90069-5.
[33] Lasaga AC. The treatment of multi-component diffusion and ion pairs in diagenetic fluxes. Am J Sci 1979;279:324-46. doi: 10.2475/ajs.279.3.324.
[34] Felmy AR, Weare JH. Calculation of multicomponent ionic-diffusion from zero to high-concentration 1. The System Na-K-Ca-Mg-Cl-SO_4-H_2O at 25-degrees-C. Geochim Cosmochim Acta 1991;55:113-31. doi: Doi 10.1016/0016-7037(91)90405-T.
[35] Boudreau BP, Meysman FJR, Middelburg JJ. Multicomponent ionic diffusion in porewaters: Coulombic effects revisited. Earth Planet Sci Lett 2004;222:653-66. doi: 10.1016/j.epsl.2004.02.034.
[36] Cussler EL. Diffusion : Mass transfer in fluid systems. 3rd ed. Cambridge University Press, Cambridge, New York 2009.
[37] Rolle M, Muniruzzaman M, Haberer CM, Grathwohl P. Coulombic effects in advection-dominated transport of electrolytes in porous media: Multicomponent ionic dispersion. Geochim Cosmochim Acta 2013;120:195-205. doi: http://dx.doi.org/10.1016/j.gca.2013.06.031.
[38] Muniruzzaman M, Haberer CM, Grathwohl P, Rolle M. Multicomponent ionic dispersion during transport of electrolytes in heterogeneous porous media: Experiments

836 and model-based interpretation. Geochim Cosmochim Acta 2014;141:656-69. doi:
837 http://dx.doi.org/10.1016/j.gca.2014.06.020.
838 [39] Muniruzzaman M, Rolle M. Impact of multicomponent ionic transport on pH fronts
839 propagation in saturated porous media. Water Resour Res 2015;51:6739-55. doi:
840 10.1002/2015WR017134.
841 [40] Rasouli P, Steefel CI, Mayer KU, Rolle M. Benchmarks for multicomponent
842 diffusion and electrochemical migration. Computat Geosci 2015;19:523-33. doi:
843 10.1007/s10596-015-9481-z.
844 [41] Bauer RD, Rolle M, Bauer S, Eberhardt C, Grathwohl P, Kolditz O, Griebler C.
845 Enhanced biodegradation by hydraulic heterogeneities in petroleum hydrocarbon plumes.
846 J Contam Hydrol 2009;105:56-68. doi: 10.1016/j.jconhyd.2008.11.004.
847 [42] Rolle M, Chiogna G, Bauer R, Griebler C, Grathwohl P. Isotopic fractionation by
848 transverse dispersion: Flow-through microcosms and reactive transport modeling study.
849 Environ Sci Tech 2010;44:6167-73. doi: 10.1021/es101179f.
850 [43] Haberer CM, Rolle M, Cirpka OA, Grathwohl P. Oxygen transfer in a fluctuating
851 capillary fringe. Vadose Zone J 2012;11. doi: 10.2136/Vzj2011.0056.
852 [44] Hochstetler DL, Rolle M, Chiogna G, Haberer CM, Grathwohl P, Kitanidis PK.
853 Effects of compound-specific transverse mixing on steady-state reactive plumes: Insights
854 from pore-scale simulations and Darcy-scale experiments. Adv Water Resour 2013;54:1-
855 10. doi: 10.1016/j.advwatres.2012.12.007.
856 [45] Ye Y, Chiogna G, Cirpka OA, Grathwohl P, Rolle M. Enhancement of plume
857 dilution in two-dimensional and three-dimensional porous media by flow focusing in
858 high-permeability inclusions. Water Resour Res 2015;51:5582-602. doi:
859 10.1002/2015WR016962.
860 [46] Fiori A, Jankovic I, Dagan G. The impact of local diffusion upon mass arrival of a
861 passive solute in transport through three-dimensional highly heterogeneous aquifers. Adv
862 Water Resour 2011;34:1563-73. doi: 10.1016/j.advwatres.2011.08.010.
863 [47] Hadley PW, Newell C. The new potential for understanding groundwater
864 contaminant transport. Groundwater 2014;52:174-86. doi: 10.1111/gwat.12135.
865 [48] LaBolle EM, Fogg GE. Role of molecular diffusion in contaminant migration and
866 recovery in an alluvial aquifer system. Trans Porous Med 2001;42:155-79. doi:
867 10.1023/A:1006772716244.
868 [49] Liu CX, Ball WP. Back diffusion of chlorinated solvent contaminants from a natural
869 aquitard to a remediated aquifer under well-controlled field conditions: Predictions and
870 measurements. Ground Water 2002;40:175-84. doi: 10.1111/j.1745-
871 6584.2002.tb02502.x.
872 [50] Chiogna G, Eberhardt C, Grathwohl P, Cirpka OA, Rolle M. Evidence of
873 compound-dependent hydrodynamic and mechanical transverse dispersion by multitracer
874 laboratory experiments. Environ Sci Tech 2010;44:688-93. doi: 10.1021/Es9023964.
875 [51] Chiogna G, Cirpka OA, Grathwohl P, Rolle M. Relevance of local compound-
876 specific transverse dispersion for conservative and reactive mixing in heterogeneous
877 porous media. Water Resour Res 2011;47:W07540. doi: 10.1029/2010wr010270.
878 [52] Rasa E, Chapman SW, Bekins BA, Fogg GE, Scow KM, Mackay DM. Role of back
879 diffusion and biodegradation reactions in sustaining an MTBE/TBA plume in alluvial
880 media. J Contam Hydrol 2011;126:235-47.
881 http://dx.doi.org/10.1016/j.jconhyd.2011.08.006.

882 [53] Rolle M, Chiogna G, Hochstetler DL, Kitanidis PK. On the importance of diffusion
883 and compound-specific mixing for groundwater transport: An investigation from pore to
884 field scale. J Contam Hydrol 2013;153:51-68.
885 http://dx.doi.org/10.1016/j.jconhyd.2013.07.006.
886 [54] Van Breukelen BM, Rolle M. Transverse hydrodynamic dispersion effects on
887 isotope signals in groundwater chlorinated solvents' plumes. Environ Sci Tech
888 2012;46:7700-8. doi: 10.1021/es301058z.
889 [55] Kitanidis PK. The concept of the Dilution Index. Water Resour Res 1994;30:2011-
890 26. doi: 10.1029/94WR00762.
891 [56] Van Cappellen P, J-F Gaillard. Biogeochemical dynamics in aquatic sediments.
892 Reviews in Mineralogy and Geochemistry. 34 (1996) 335-76.
893 [57] Liu CX, Zachara JM, Felmy AR, Gorby Y. An electrodynamics-based model for ion
894 diffusion in microbial polysaccharides. Colloids Surf A and B 2004:38:55-65. doi:
895 10.1016/j.colsurfb.2004.08.003.
896 [58] Alizadeh A, Zhang L, Wang MR. Mixing enhancement of low-Reynolds electro-
897 osmotic flows in microchannels with temperature-patterned walls. J Colloid Interface Sci
898 2014;431:50-63. doi: 10.1016/j.jcis.2014.05.070.
899 [59] Zhang L, Wang MR. Modeling of electrokinetic reactive transport in micropore
900 using a coupled lattice Boltzmann method. J Geophys Res-Sol Ea 2015;120:2877-90. doi:
901 10.1002/2014JB011812.
902 [60] Bard AJ, Faulkner LR. Electrochemical methods fundamentals and applications.
903 (2nd ed.). John Wiley, New York 2001:718.
904 [61] Cirpka OA, Frind EO, Helmig R. Streamline-oriented grid generation for transport
905 modelling in two-dimensional domains including wells. Adv Water Resour 1999;22:697-
906 710. doi: 10.1016/s0309-1708(98)00050-5.
907 [62] Guedes de Carvalho JRF, Delgado JMPQ. Overall map and correlation of dispersion
908 data for flow through granular packed beds. Chem Eng Sci 2005;60:365-75. doi:
909 http://dx.doi.org/10.1016/j.ces.2004.07.121.
910 [63] Rolle M, Hochstetler DL, Chiogna G, Kitanidis PK, Grathwohl P. Experimental
911 investigation and pore-scale modeling interpretation of compound-specific transverse
912 dispersion in porous media. Trans Porous Med 2012;93:347-62. doi: 10.1007/s11242-
913 012-9953-8.
914 [64] Archie GE. The electrical resistivity log as an aid in determining some reservoir
915 characteristics. Trans AIME; 146.
916 [65] Boving TB, P Grathwohl. Tracer diffusion coefficients in sedimentary rocks:
917 correlation to porosity and hydraulic conductivity. J Contam Hydrol 2001; 53:85-100.
918 doi: Doi 10.1016/S0169-7722(01)00138-3.
919 [66] Scheidegger AE. General theory of dispersion in porous media. Journal of Geophys
920 Res 1961;66:3273-8. doi: 10.1029/JZ066i010p03273.
921 [67] Bijeljic B, Muggeridge AH, Blunt MJ. Pore-scale modeling of longitudinal
922 dispersion. Water Resour Res 2004;40:W11501. doi: 10.1029/2004wr003567.
923 [68] Hazen A. Some physical properties of sands and gravels: with special reference to
924 their use in filtration. Ann Rep State Board of Health Mass 1892;24:541-556.
925 [69] Eckert D, Rolle M, Cirpka OA. Numerical simulation of isotope fractionation in
926 steady-state bioreactive transport controlled by transverse mixing. J Contam Hydrol
927 2012;140–141:95-106. doi: http://dx.doi.org/10.1016/j.jconhyd.2012.08.010.

928 [70] Cirpka OA, Frind EO, Helmig R. Numerical methods for reactive transport on
929 rectangular and streamline-oriented grids. Adv Water Resour 199;22:711-28.
930 http://dx.doi.org/10.1016/S0309-1708(98)00051-7.
931 [71] Davis T, Duff I. An unsymmetric-pattern multifrontal method for sparse LU
932 factorization. SIAM J Matrix Anal 1997;18:140-58. doi: 10.1137/S0895479894246905.
933 [72] Leij FJ, Skaggs TH, van Genuchten MT. Analytical solutions for solute transport in
934 three-dimensional semi-infinite porous media. Water Resour Res 1991;27:2719-33. doi:
935 10.1029/91WR01912.
936 [73] van Genuchten MT, Leij FJ, Skaggs TH, Toride N, Bradford SA, Pontedeiro EM.
937 Exact analytical solutions for contaminant transport in rivers 1. The equilibrium
938 advection-dispersion equation. J Hydrol Hydromech 2013;61:146-60. doi: 10.2478/johh-
939 2013-0020.
940 [74] Lasaga AC. Kinetic theory in the earth sciences. Princeton University Press,
941 Princeton, N.J 1998.
942 [75] Tartakovsky AM, Redden G, Lichtner PC, Scheibe TD, Meakin P. Mixing-induced
943 precipitation: Experimental study and multiscale numerical analysis. Water Resour Res
944 2008;44:W06s04. doi: 10.1029/2006wr005725.
945 [76] Rolle M, Eberhardt C, Chiogna G, Cirpka OA, Grathwohl P. Enhancement of
946 dilution and transverse reactive mixing in porous media: Experiments and model-based
947 interpretation. J Contam Hydrol 2009;110:130-42. doi: 10.1016/j.jconhyd.2009.10.003.
948 [77] Rolle M, Kitanidis PK. Effects of compound-specific dilution on transient transport
949 and solute breakthrough: A pore-scale analysis. Adv Water Resour 2014;71:186-99.
950 http://dx.doi.org/10.1016/j.advwatres.2014.06.012.
951 [78] Sudicky EA. A natural gradient experiment on solute transport in a sand aquifer:
952 Spatial variability of hydraulic conductivity and its role in the dispersion process. Water
953 Resour Res 1986;22:2069-82. doi: 10.1029/WR022i013p02069.
954 [79] Dykaar BB, Kitanidis PK. Determination of the effective hydraulic conductivity for
955 heterogeneous porous media using a numerical spectral approach: 1. Method. Water
956 Resour Res. 1992;28:1155-66. doi: 10.1029/91WR03084.
957 [80] Yang C, J Samper. Numerical evaluation of multicomponent cation exchange
958 reactive transport in physically and geochemically heterogeneous porous media.
959 Computat Geosci 2009;13:391-404. doi: 10.1007/s10596-009-9127-0.
960 [81] Christiansen JS, Engesgaard PK, Bjerg PL. A physically and chemically
961 heterogeneous aquifer: field study and reactive transport modelling. In: Groundwater
962 Quality: Remediation and Protection, Proceedings of the GQ'98 Conference, IAHS Press,
963 Wallingford 1998:329-36.
964 [82] Jacques D, Mouvet C, Mohanty B, Vereecken H, Feyen J. Spatial variability of
965 atrazine sorption parameters and other soil properties in a podzoluvisol. J Contam Hydrol
966 1999;36:31-52. http://dx.doi.org/10.1016/S0169-7722(98)00141-7.
967 [83] Samper J, Yang C. Stochastic analysis of transport and multicomponent competitive
968 monovalent cation exchange in aquifers. Geosphere 2006;2:102-12. doi:
969 10.1130/ges00030.1.
970 [84] Kjøller C, Postma D, Larsen F. Groundwater acidification and the mobilization of
971 trace metals in a sandy aquifer. Environ Sci Tech 2004;38:2829-35. doi:
972 10.1021/es030133v.

973 [85] Prigiobbe V, Bryant SL. pH-dependent transport of metal cations in porous media.
974 Environ Sci Tech 2014;48:3752-9. doi: 10.1021/es403695r.
975 [86] Li L, Salehikhoo F, Brantley SL, Heidari P. Spatial zonation limits magnesite
976 dissolution in porous media. Geochim Cosmochim Acta 2014;126:555-73.
977 http://dx.doi.org/10.1016/j.gca.2013.10.051.
978 [87] Molins S, Trebotich D, Steefel CI, Shen CP. An investigation of the effect of pore
979 scale flow on average geochemical reaction rates using direct numerical simulation.
980 Water Resour Res 2012;48:W03527. doi: 10.1029/2011wr011404.
981 [88] Haberer CM, Muniruzzaman M, Grathwohl P, Rolle M. Diffusive/Dispersive and
982 reactive fronts in porous media: Fe (II)-Oxidation at the unsaturated/saturated interface.
983 Vadose Zone J 2015;14(5). doi: http://dx.doi.org/10.2136/vzj2014.07.0091.
984 [89] Fakhreddine S, Lee J, Kitanidis PK, Fendorf S, Rolle M. Imaging geochemical
985 heterogeneities using inverse reactive transport modeling: An example relevant for
986 characterizing arsenic mobilization and distribution. Adv Water Resour 2016;88: 186-97.
987 http://dx.doi.org/10.1016/j.advwatres.2015.12.005.
988 [90] Redden G, Fox D, Zhang C, Fujita Y, Guo L, Huang H. $CaCO_3$ precipitation,
989 transport and sensing in porous media with in situ generation of reactants. Environ Sci
990 Tech 2014;48:542-9. doi: 10.1021/es4029777.
991 [91] Chiogna G, Rolle M, Bellin A, Cirpka OA. Helicity and flow topology in three-
992 dimensional anisotropic porous media. Adv Water Resour 2014;73:134-43.
993 http://dx.doi.org/10.1016/j.advwatres.2014.06.017.
994 [92] Ye Y, G Chiogna, OA Cirpka, P Grathwohl, M Rolle. experimental evidence of
995 helical flow in porous media. Phys Rev Lett 2015;115:194502. doi:
996 10.1103/Physrevlett.115.194502.
997 [93] Cirpka OA, Chiogna G, Rolle M, Bellin A. Transverse mixing in three-dimensional
998 nonstationary anisotropic heterogeneous porous media. Water Resour Res 2015;51:241-
999 60. doi: 10.1002/2014WR015331.

1000